Test particle orbits around regular black holes in general relativity combined with nonlinear electrodynamics

Javlon Rayimbaev,[1,2,3,*] Marcos Figueroa,[4,†] Zdeněk Stuchlík,[5,‡] and Bakhtinur Juraev[5,§]

[1]*Ulugh Beg Astronomical Institute, Astronomicheskaya 33, Tashkent 100052, Uzbekistan*
[2]*National University of Uzbekistan, Tashkent 100174, Uzbekistan*
[3]*Institute of Nuclear Physics, Ulughbek, Tashkent 100214, Uzbekistan*
[4]*California State University, 9001 Stockdale Hwy, Bakersfield, California 93311, USA*
[5]*Research Centre for Theoretical Physics and Astrophysics, Institute of Physics, Silesian University in Opava, Bezručovo nám.13, CZ-74601 Opava, Czech Republic*

(Received 3 January 2020; revised manuscript received 26 March 2020; accepted 16 April 2020; published 26 May 2020)

We provide detailed analysis of the curvature structure of the spacetime around regular black holes (RBHs) governed by general relativity (GR) combined with nonlinear electrodynamics (NED), characterized by electric charge Q, and degree of nonlinearity n. We consider special class of the backgrounds introduced by Toshmatov *et al.* [Phys. Rev. D **98**, 028501 (2018)] that have proper Maxwell weak-field limit of the NED sector. We also study the motion of uncharged and charged particles in the RBH background. We determine shadows of such black holes (BHs) using the effective geometry governing motion of photons in the background of NED RBHs. The analysis of circular motion enables to determine innermost stable circular orbits (ISCO) and marginally bound orbits (MBO). We show that the radius of ISCO and MBO for neutral particles decreases as the parameters of the RBH Q and n increase for the fixed value of the BH mass. We demonstrate that for the electrically charged particles properties of the circular orbits strongly depend on their Coulomb interaction with the RBH charge. The dependence of the ISCO radius on the particle specific charge q and the RBH parameters is rather complex, but for the attractive Coulomb interaction there is a general feature (independent of n) giving a limiting value of the intensity of this interaction $qQ_{\max}$ behind which no stable circular orbits are allowed around the RBH. Comparison of the RBH with Reissner-Nordström black holes (RNBH) shows that for the same electric charges of these backgrounds the location of the relevant orbits is at substantially smaller radii for the RBH, demonstrating thus a strong influence of the NED effects. The analysis of ISCO radius of test particles has shown that the charge of RBH Q can mimic the rotation parameter of Kerr BH up to the value $a = 0.8M$. We have also shown that the RN BH charge can mimic the rotation parameter up to $a = 0.5M$ and the RBH charge up to $Q = 0.2M$. Applications from observational data to the parameters of the supermassive black holes (SMBHs) at the galactic center Messier 87 (M87) and Milky Way so called Sagittarius A* (Sgr A^*) give the mimic value for the RBH charge parameter for the rotation parameter of M87 to be $10^3 Q \approx 277.56^{+3.82}_{-1.26}$, while for Sgr A^* there is $10^3 Q \approx 187.33^{+27.6}_{-26.4}$. Moreover, it is shown that the RN BH charge cannot mimic the rotation parameter of the SMBH M87, however, it can mimic the spin parameter of Sgr A^* at $10^3 Q_{\rm RN}/M = 828.71^{+70.58}_{-60.94}$.

DOI: 10.1103/PhysRevD.101.104045

I. INTRODUCTION

The solutions of the Einstein field equations for electrically and magnetically charged black holes were first obtained by H. Reissner in 1916 (the same year as the Schwarzschild solution) [2] and independently by G. Nordström in 1918 [3]. The solution, governed by general relativity (GR) coupled with linear Maxwell electrodynamics, describes a Reissner-Nordström black hole (RNBH) which has physical singularity at it's center ($r = 0$). However, there are other exact solutions for electrically and magnetically charged black holes which avoid this physical singularity by coupling GR to nonlinear electrodynamics (NED)—such solutions are called RBH solutions.[1] Several types of the RBH solutions have been

*javlon@astrin.uz
†mfigueroa347@gmail.com
‡zdenek.stuchlik@fpf.slu.cz
§bahti-bahti@mail.ru

[1]For the Maxwell electrodynamics, the spacetime structure of the RNBHs is modified in the same way for both the electric and magnetic charges [4], but it is not so in the case of NED [5].

introduced by in the past [5–13] being based on various Lagrangians governing the NED; their electromagnetic and thermodynamic properties, particle dynamics around them have been studied by many authors [14–27].

Do charged BHs exist in the Universe? In principle this is possible, but we expect that the realistic BHs can have limited charge due to preferred accretion of oppositely charged particles from orbiting plasma [28], of course this argument is not relevant for hypothetical magnetically charged BHs [29,30]. Recently, the electric charge of the SMBH SgrA* situated in the center of the Milky Way has been estimated through observational data [31–33] and concluded that the charge has to be small charge and can contribute to the BH geometry only slightly, but the electromagnetic interaction of the orbiting charged particles with the allowed BH electric charge can be relevant for the optical phenomena recently observed by the GRAVITY [34].

In order to understand the electromagnetic phenomena arising in vicinity of BHs, it is important to study basic properties of the charged particle motion. Such studies properly reflect the character of the combined gravitational and electromagnetic fields related to charged BHs and give insight into the processes in ionized accretion disks [35–41]. A number of authors have considered the charged particles (or uncharged particle) motion around charged BHs: (a) BHs immersed in a magnetic field [37,42–49]; (b) RNBHs [50–56]; magnetized particles around a BH immersed in an external asymptotically uniform magnetic field [57–62].

Testing the general relativity and alternative theories of gravity due to studies of motion of particles around BHs with different parameters may help to obtain constrains on the astrophysical BH parameters such as spin and charge from the observational data. However, the parameters estimated due to the ISCO of the particle motion around the BH and the shadow of the BH, may be predicted the same in different theories of gravity. In such cases we cannot distinguish the character of the astrophysical BH, as the parameters of different theories of gravities may mimic each other [63]. Recently, several authors obtained constraints on the parameters of the SMBHs situated in the Galaxy center, and the galaxy M87, located at the distance about 17 Mpc from the solar system, using observational data from physical evidences around them, such as shadow of the BH M87 obtained by the EHT and [30,64–68]. Recently, authors of Ref. [69] have shown that magnetically charged RBH can mimic rotation parameter up to $Q_m/M < 0.7$ through analysis of the SMBH M87 shadow considered in the framework of the Einstein-Bronnikov model.

Here, we aim to study properties of the electrically charged RBH solution obtained in [1] and to describe the characteristic orbits of massless, as well as, massive, charged and neutral particles around it and to obtain values of the electric charge parameter that mimic the rotation parameter of the SMBHs M87 and SrgA*. We have chosen the case of the generic regular black holes governed by the Lagrangian introduced in [1,11] that covers the regular Bardeen and Hayward black hole spacetimes as special cases. We focus attention to the special class of regular spacetimes having the correct Maxwell weak-field limit predicting in its simplest form optical phenomena related to Keplerian disks in accord with observations [70], contrary to the those related to disks orbiting the Bardeen regular spacetimes that are in strong contradiction with the observations [71,72]. The Maxwellian NED RBHs are thus worth of detailed studies in relation to the electromagnetic effects in their vicinity.

The paper is organized as follows: Sec. II is devoted to the curvature invariants, event horizon and electric field properties of the spacetime around the RBH, in Sec. III we considered photon and neutrinolike particle orbits around the RBH, in Sec. IV the motion of massive test particles around the RBH was studied, in Sec. V we have investigated the motion of electrically charged particles, and, in particular, the ISCO and MBO is studied in detail. In Sec. VI we have focused on the mimicker values for the charge parameter Q as related to the spin parameter of the SMBHs M87 and Sgr A^*, considering them as a RBH (RN BH) and applying the studies of ISCO for neutral particles and photon circular orbits governing the black hole shadow in Secs. III and IV. In Sec. VII we have summarized the obtained results.

Throughout this work we use signature $(-,+,+,+)$ for the spacetime and geometric unit system $G = c = 1$. (However, for astrophysical applications we use standard units in our expressions). Latin indices run from 1 to 3 and Greek ones from 0 to 3.

II. MAXWELLIAN NED REGULAR BLACK HOLES

The generic RBH spacetimes [1,11] are solutions of GR coupled to NED determined by the action taking the form

$$S = \frac{1}{16\pi}\int dx^4\sqrt{-g}(R - L(F)) \tag{1}$$

where $F = F^{\mu\nu}F_{\mu\nu}$ is the invariant of the electromagnetic field tensor $F_{\mu\nu} = A_{\nu,\mu} - A_{\mu,\nu}$ expressed by using the electromagnetic field potential A_μ.

The generic RBH spacetimes are governed by the electromagnetic Lagrangian being a function of the electromagnetic field invariant taking the form

$$L(F) = \frac{4n}{\alpha}\frac{(\alpha F)^{\frac{k+3}{4}}}{\left[1 + (\alpha F)^{\frac{k}{4}}\right]^{1+\frac{n}{k}}}. \tag{2}$$

The Maxwellian NED generic RBH spacetimes having the proper Maxwell weak-field limit are the solutions of GR

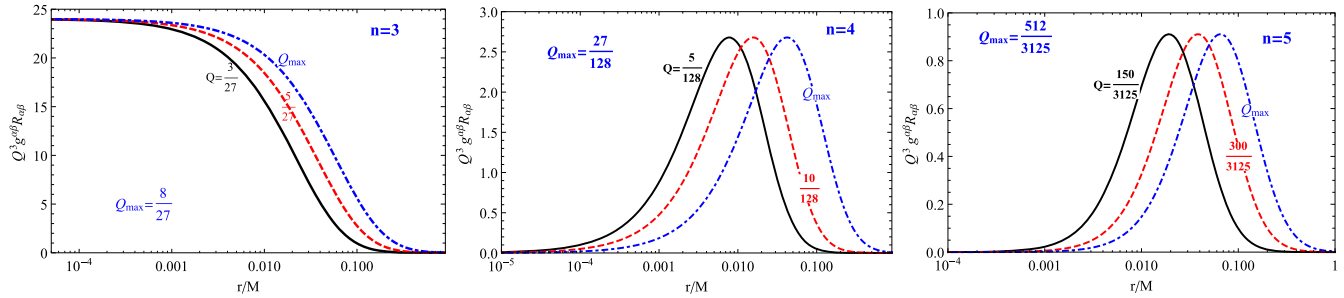

FIG. 1. Radial dependence of Ricci scaler for different values of the RBH parameters Q and n.

combined with NED represented by special class of the NED Lagrangian given by the parameters $k = 1$ and $n \geq 3$, where n is assumed to be an integer [1,73]. The metric tensor of such spherically symmetric spacetimes

$$ds^2 = -f dt^2 + f^{-1} dr^2 + r^2 d\Omega^2 \tag{3}$$

is then represented by the lapse function that can be expressed in the form [73]

$$f = 1 - \frac{2M}{r}\left(1 + \frac{Q}{r}\right)^{-n}, \tag{4}$$

where $Q > 0$ denotes charge of the black hole and M its mass. For $Q = 0$ we obtain the Schwarzschild vacuum spacetime. The last RBH parameter n reflects degree of the electrodynamic nonlinearity; recall that the parameter k is fixed to $k = 1$ guaranteeing the proper Maxwell weak-field limit of the generic NED framework. The term $d\Omega^2 = d\theta^2 + \sin^2\theta d\varphi^2$ is the angular part of the spherically symmetric spacetime.

The four-potential of the Maxwellian NED RBH electromagnetic field [1] reads

$$A_\mu = \frac{n}{\sqrt{2\alpha}} \frac{\frac{Q}{r}}{(1+\frac{Q}{r})^{n+1}} \left[1 + (3-n)\frac{Q}{r}\right] \{1,0,0,0\} \tag{5}$$

where α is a constant reflecting the intensity of the interaction [1,11] which we have chosen to be $\alpha = n^2/2$ for simplicity and in the weak-field limit A_t in Eq. (5) takes the form of the RN potential $\varphi_{\rm RN} = Q/r$.

A. Curvature of RBH

Studies of curvature invariants such as the Ricci scalar, square of the Ricci tensor and the Kretschmann scalar help to deeply understand properties of a given spacetime. We thus investigate the curvature invariants of the metric (4).

1. The Ricci scalar

We first give the Ricci scalar of the spacetime determined by the metric (4) that can be expressed as

$$R = g^{\mu\nu} R_{\mu\nu} = 2n(n+1)\frac{Q^2}{r^5}\left(1 + \frac{Q}{r}\right)^{-(n+2)}. \tag{6}$$

In the limiting case $Q = 0$, $R = 0$ and the matter (field) inside the inner horizon does not give rise to the existence of the Ricci scalar, as this is the vacuum solution of GR where the Ricci tensor vanishes by definition. The limits of the Ricci scalar at the center read

$$\lim_{r\to 0} R_{(n=3)} = \frac{24}{Q^3}, \qquad \lim_{r\to 0} R_{(n\geq 4)} = 0. \tag{7}$$

We study the radial dependence of the Ricci scalar by varying the RBH parameters, Q and n, keeping fixed M. One can see from Eq. (6) that the dimensions of the scalar are $1/[Q]^3$. We considered the dimensionless Ricci scalar curvature, multiplying the Ricci scalar by Q^3.

Figure 1 shows the radial dependence of the dimensionless Ricci scalar on different values of Q and n. One can see from the figure that increasing n decreases the value of the dimensionless Ricci scalar and increasing the value of Q shifts the maximum value of the curvature out from the center of the RBH. For example, in the case of $n = 3$, there is finite Ricci scalar at the center of the BH—this means that the RBH is not flat nor has a singular point at its center. In the cases $n \geq 4$, the Ricci scalar is vanishing at the center of the BH and at the inner horizon—the radial profile of the Ricci scalar is represented in this cases by a "Gaussian" distribution. We can conclude that in the case $n = 3$ the charged matter is denser in the center (but not infinite), and in the cases where $n \geq 4$, the charged matter distribution is "Gaussian-like". This means that matter is organized in a shell-like manner inside of the RBH which could correspond to the charged matter distribution in the shell. As the size of the shell becomes larger, the maximum of the distribution shifts outside while both parameters of the RBH, Q and n, increase. However the maximum value does not vary with varying the parameter Q for a fixed n. One can conclude that the Ricci scalar corresponds to the electrostatic field, which is related to the total charge of the RBH.

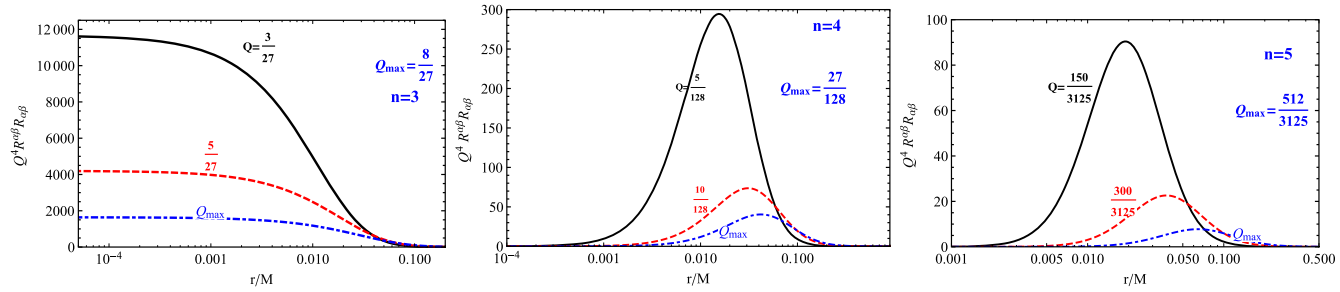

FIG. 2. Dimensionless $\mathcal{R}$ scalar as a function of dimensionless radial coordinate (r/M) for different values of the RBH parameters Q and n.

2. The square of Ricci tensor

The second curvature invariant we consider is the square of the Ricci tensor, $\mathcal{R}$, related to the lapse function given by Eq. (4). This invariant is given by the relation

$$\mathcal{R} = R_{\mu\nu}R^{\mu\nu} = \left(\frac{M}{r^3}\frac{nQ}{r}\left(1+\frac{Q}{r}\right)^{-(n+2)}\right)^2 \times 2\left[8-4(n-3)\frac{Q}{r}+(n^2-2n+5)\frac{Q^2}{r^2}\right]. \quad (8)$$

In the case of $Q = 0$ (the Schwarzschild case) we again arrive to $\mathcal{R} = 0$ due to the fact that vacuum spacetimes in GR are Ricci flat. The limits of the $\mathcal{R}$ scalar curvature read

$$\lim_{r\to 0}\mathcal{R}_{(n=3)} = \frac{144M^2}{Q^6}, \qquad \lim_{r\to 0}\mathcal{R}_{(n\geq 4)} = 0 \quad (9)$$

and we expect similar qualitative behavior as in the case of the Ricci scalar, namely the Gaussian behavior of the radial profiles of the square of the Ricci tensor for $n \geq 4$.

The properties of $\mathcal{R}$ for different values of the RBH parameters Q and n are reflected in Fig. 2 demonstrating the radial profiles of a dimensionless $\mathcal{R}$. One can see from the figures that the properties of the square of the Ricci tensor is very similar to those of the Ricci scalar, with respect to the values of parameter n. However, the maximal value of the dimensionless scalar strongly depends on the values of the RBH parameters. Moreover, increasing of the values of the RBH parameters decreases the maximum value of the square of Ricci tensor. In cases where $n \geq 4$ the maximum value shifts out from the center of RBH.

3. The Kretschmann scalar

The third scalar we study is the Kretschmann scalar, enabling us to obtain more information about the character of the curvature of spacetime metric governed by the lapse function (4). It should be stressed that this is the only curvature scalar of those considered here that is reflecting the curvature of the vacuum spacetime solutions of GR that generally Ricci flat solutions.

The expression for the Kretschmann scalar of the considered RBH spacetimes takes the form

$$K = R_{\mu\nu\sigma\delta}R^{\mu\nu\sigma\delta} = \frac{4M^2}{r^6}\left(1+\frac{Q}{r}\right)^{-2(n+2)} \times \left[12-24(n-2)\frac{Q}{r}+4n(6n+1)\frac{Q^2}{r^2} - 8(n^3-5n^2+8n-6)\frac{Q^3}{r^3} + (n^4-6n^3+17n^2-20n+12)\frac{Q^4}{r^4}\right] \quad (10)$$

and it is reduced to the Schwarzschild BH spacetime form $K = 48M^2/r^6$ for $Q = 0$.

The central limits $(r = 0)$ of the Kretschmann scalar read

$$\lim_{r\to 0}K_{(n=3)} = \frac{96M^2}{Q^6}, \qquad \lim_{r\to 0}K_{(n\geq 4)} = 0. \quad (11)$$

In general, one can see that the root of the Kretschmann scalar can be interpreted as a matter energy density, $\sqrt{K} \sim \rho_{\mathrm{M}}$. The units of the Kretschmann scalar is $1/[Q]^4$, and here we also analyze the dimensionless scalar by multiplying it by a factor Q^4.

Figure 3 illustrates the profiles of the dimensionless Kretschmann scalar for different values of n and Q. One can see from the figure that the distribution of the Kretschmann scalar is very similar to the distribution of the square of the Ricci tensor.

As the charge of the RBH increases the value of the Kretschmann scalar decreases and for $n = 3$ there is finite value of the scalar in the center of the RBH, and for the cases $n \geq 4$ in the center the value of the scalar is zero. In the case of $n \geq 4$ the maximum of the curvature shifts outside for larger values of the RBH charge Q.

As we mentioned above, the Kretschmann scalar corresponds to the total matter-energy density, and when the value of Q increases, as seen from Fig. 3, the value of the Kretschmann scalar decreases.

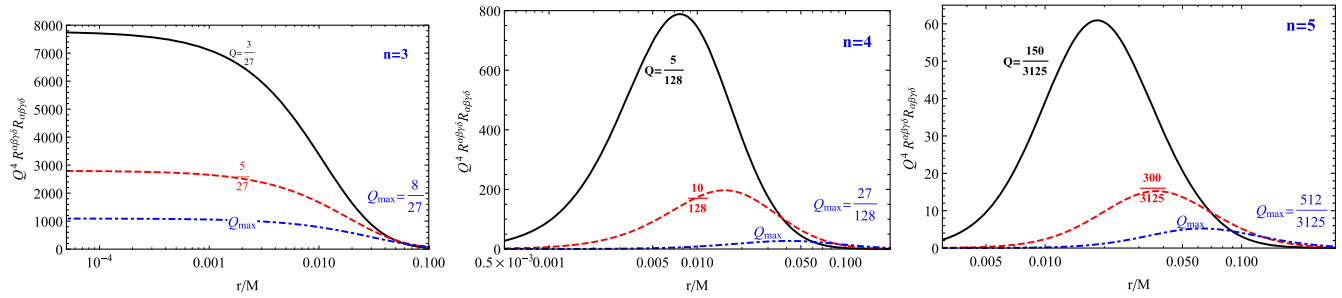

FIG. 3. Dimensionless Kretschmann scalar as a function of dimensionless radial coordinate (r/M) for different values of the RBH parameters Q and n.

B. Horizons of the RBH

Now we study properties of the RBH spacetimes, governed by the lapse function given by Eq. (4), by determining the existence and positions of their event horizons.

The standard way to find the event horizon is by setting $g_{rr} \to \infty$, $g^{rr} = 0$, or equivalently $f = 0$. In our case the existence ad position of the event horizons depends on the RBH parameters n and Q, if we put $M = 1$, or equivalently, we use dimensionless coordinates r/M and charges Q/M. Calculating the event horizons by setting $f = 0$ shows that:

(i) two event horizons exists for $Q < Q_{\text{ext}}$: an inner and an outer horizon

(ii) for $Q = Q_{\text{ext}}$ we have an extreme RBH with maximal allowed charge, where the two event horizons coalesce forming a single event horizon, (r_h^{ext}), instead of two (see, Fig. 4)

(iii) when $Q > Q_{\text{ext}}$ we have no-horizon strong gravity objects, having no event horizon (the lapse function is positive everywhere in the range $0 < r < \infty$).

In order to find the value of the extreme charge (Q_{ext}) and the corresponding event horizon r_h^{ext} of the RBH, we established the system of equations $f = 0$ and $f' = 0$, where we solved the system of equations simultaneously for given values of n. We then obtained the event horizon and the extreme value for the RBH. The extreme charge of the RBH depends on the degree n, for example when $n = 3$, $Q_{\text{ext}}^{(3)} = \frac{8}{27}M$ and for $n = 4$, $Q_{\text{ext}}^{(4)} = \frac{27}{128}M$. In Fig. 5 we show the dependence of the extreme charge, Q_{ext}, a RBH can have, on the nonlinearity degree parameter n. One can see that the value of Q_{ext} decreases as n increases, and when $n \gg 3$, $Q_{\text{ext}} \ll M$. Figure 5 also shows that a charged RBH can exist for $Q \leq Q_{\text{ext}}$, otherwise the geometry corresponds to a no-horizon strong gravity object.

We can say due to Fig. 4 that as the charge of the RBH, Q, and the degree, n, both increase, the radius of the inner event horizon becomes larger and the outer event horizon of the radius becomes smaller. The disappearance of the event

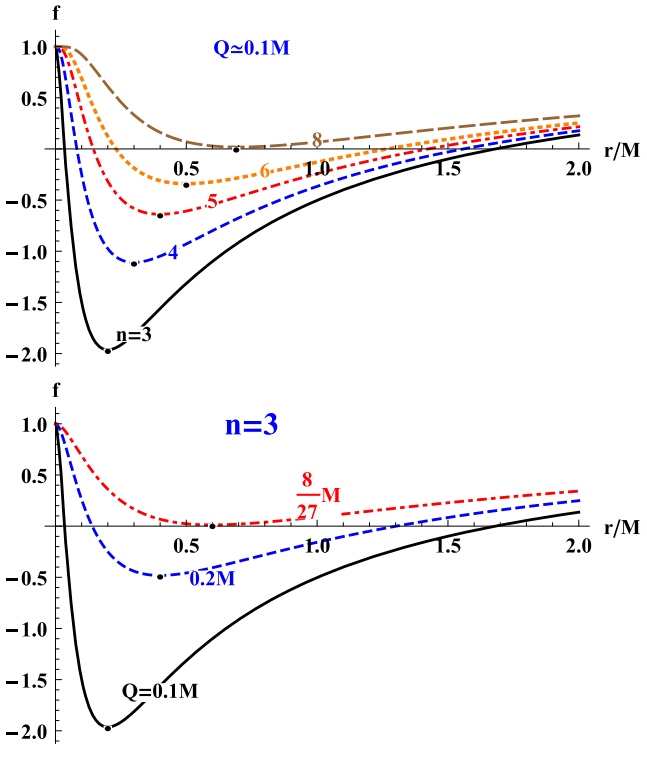

FIG. 4. Lapse function f as a function of dimensionless radial coordinates r/M, with different values of Q and n, the black dots indicates the minimum of the lapse function.

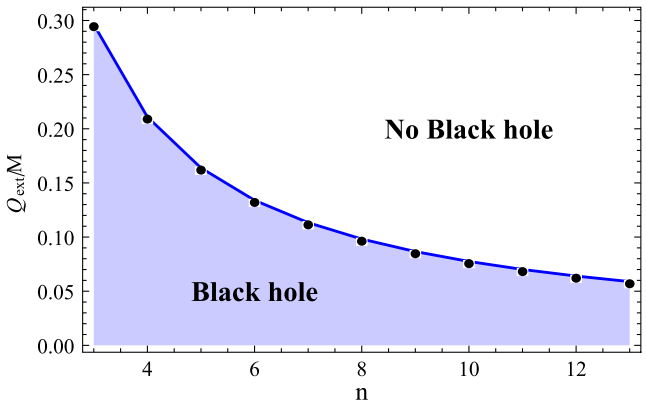

FIG. 5. Values of extreme charge of RBH Q_{ext} for different values of the degree n.

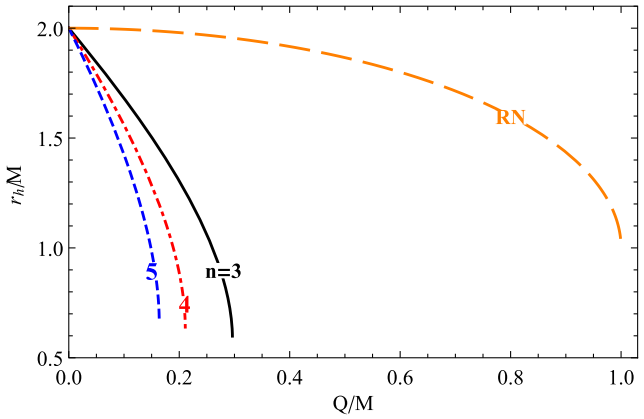

FIG. 6. The dependence of the outer event horizon radius on BH charge Q for fixed values of $n = 3, 4, 5$. For comparison we include also the case of the RNBHs.

horizon of the RBH when $Q > Q_{\rm ext}$ results in a no-horizon strong gravity object.

The expressions of the event horizon radius for $n = 3$ and $n = 4$ are given, respectively, by the relations

$$\frac{ar_h^{(3)}}{M} = \frac{1}{4}(a+2)^2 + (a+3)\frac{Q}{M} \tag{12}$$

$$\frac{2r_h^{(4)}}{M} = 1 + b - \frac{2Q}{M} + \sqrt{c + \frac{3}{b}\left[1 - \frac{6Q}{M}\left(1 + \frac{Q}{M}\right)\right]} \tag{13}$$

where the constants are

$$\begin{aligned} a^3 &= 8 - \frac{9Q}{M}\left(4 - \frac{3Q}{M}\right) + \frac{27Q}{M}\sqrt{\frac{Q}{M}\left(\frac{Q}{M} - \frac{8}{27}\right)} \\ b^2 &= 1 - \frac{4Q}{M} + \frac{Q}{M}\left(\frac{2Q}{M}\right)^{1/3} + \frac{4Q}{3M}\left(\frac{2Q^2}{dM^2}\right)^{1/3} \\ c &= 1 - \frac{4Q}{M} - \frac{Q}{M}\left(\frac{dQ}{36M}\right)^{1/3} - \frac{2Q}{M}\left(\frac{4Q^2}{3dM^2}\right)^{1/3} \\ d &= 1 + \sqrt{1 - \frac{128Q}{27M}}. \end{aligned} \tag{14}$$

One can see from Eqs. (12)–(14) that when $Q = 0$, the Schwarzschild case, the equation become $r_h = 2M$.

Figure 6 shows the dependence of the event horizon on the parameter Q for fixed values of n. One can see that the radius of the event horizon decreases as the value of the parameter Q increase for any fixed value of n, and the rate of this decrease increases with increasing n. For a given charge parameter, the outer event horizon of any RBH is smaller than those of the corresponding RNBH. In this figure, we have not shown the inner horizon, as it is not relevant astrophysically. However, it is possible to deduce from Fig. 4 that the both horizon radii increase as the charge Q and the degree n are increased.

C. The electric field of the RBH

The nonzero components of the electromagnetic field tensor are given by $F_{rt} = A_{t,r}$. Using the relation $E_\alpha = F_{\alpha\beta}u^\beta$, where u^β is the four velocity of the frame of an observer, we calculate the radial component of the electric field for the static observers with four-velocity $u^\alpha_{\rm PO} = f^{-1}\{1, 0, 0, 0\}$ as

$$E_{\hat{r}} = \frac{Q}{r^2}\left(1 + \frac{Q}{r}\right)^{-(n+2)} \times \left[1 - 3(n-2)\frac{Q}{r} + (n-3)(n-1)\frac{Q^2}{r^2}\right]. \tag{15}$$

One can expand Eq. (15) for different values of the parameter n, for instance $n = 3$ and $n = 4$, obtaining the relations

$$\begin{aligned} E^{n=3}_{\hat{r}} &= -\frac{Q}{r^2} + \frac{8}{r}\frac{Q^2}{r^2} - \frac{30}{r}\frac{Q^3}{r^3} + \mathcal{O}\left(\frac{Q^4}{r^4}\right) \\ E^{n=4}_{\hat{r}} &= -\frac{Q}{r^2} + \frac{12}{r}\frac{Q^2}{r^2} - \frac{60}{r}\frac{Q^3}{r^3} + \mathcal{O}\left(\frac{Q^4}{r^4}\right). \end{aligned} \tag{16}$$

Equation (16) yields the electric field around a RNBH in the linear approximation.

Figure 7 illustrates the strength of the electric field as a function of the radial distance from the BH center for different values of the parameters Q and n under the

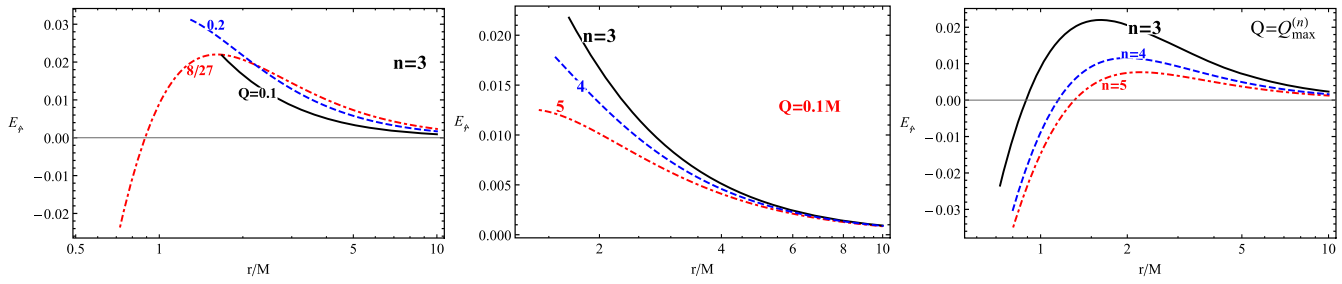

FIG. 7. Radial components of the electric field a function of radial coordinates, in the distances $r > r_{\rm h}$, in different values of Q and n.

condition that $r > r_h$. The left panel of the figure illustrates the behavior of the magnitude of the **E** field for fixed n and several properly selected values of Q. On the other hand, the cases of fixed Q and increasing values of n, as illustrated in the middle and rightmost panels, demonstrate the maximum value of the **E** field to increase, and as $Q \to Q_{\rm ext}$ the strength of the electric field decreases for larger values of n.

The only nonzero component of the electromagnetic field tensor is $F_{\rm rt}$ and the electromagnetic invariants of the electric field reads

$$F = F_{\rm rt}F^{\rm rt} = -A_{\rm t,r}^2 = -\frac{Q^2}{r^4}\left(1+\frac{Q}{r}\right)^{-2(n+2)} \times \left[1-3(n-2)\frac{Q}{r}+(n-1)(n-3)\frac{Q^2}{r^2}\right]^2 \quad (17)$$

III. THE MOTION OF MASSLESS PARTICLES

The motion of massless particles (with rest mass-energy $m = 0$ that can be approximated by neutrinos) is governed by the null geodesics of the NED RBH spacetimes, but with an exception of photons because of the nonlinearity of the electromagnetic field. However, the photon motion is in this case governed by null geodesics of the so-called effective geometry [71,74] reflecting directly the NED effects, in addition to those hidden in the spacetime structure.

A. The photon-sphere around a RBH

The photon motion in the RBH spacetimes governed by the lapse function given by Eq. (4) can be determined by the null geodesics of the effective geometry introduced in [63,71–75]

$$\tilde{g}^{\mu\nu} = g^{\mu\nu} - 4\frac{L_{FF}}{L_F}F^{\lambda}_{\mu}F^{\mu\nu} \quad (18)$$

$$\tilde{g}_{\mu\nu} = 16\frac{L_{\rm FF}F_{\mu\eta}F^{\eta}_{\nu} - (L_{\rm F}+2FL_{\rm FF})g_{\mu\nu}}{F^2L_{\rm FF}^2 - 16(L_{\rm F}+FL_{\rm FF})^2} \quad (19)$$

where

$$L_{\rm F} = \frac{\partial L(F)}{\partial F}, \qquad L_{\rm FF} = \frac{\partial^2 L(F)}{\partial F^2}. \quad (20)$$

The eikonal equation for photons in the effective geometry related to the NED RBH can be written as

$$\tilde{g}_{\mu\nu}k^{\mu}k^{\nu} = 0 \quad (21)$$

where k^{μ} is the four-wave-vector related to the four-momentum of photons by $p^{\mu} = \hbar k^{\mu}$ (in Gaussian units $\hbar = 1$). Using the results of [70,71,75], the effective potential for the photon motion in the effective geometry corresponding to the Maxwellian NED RBHs is related to the inverse of the impact parameter of photon motion in the equatorial plane, $b = p_{\phi}/p_t$, and reads

$$V_{\rm eff} = \frac{f}{r^2}\left(1+2\frac{L_{\rm FF}}{L_{\rm F}}F\right). \quad (22)$$

For details of the photon motion in Maxwellian NED RBH spacetimes with the parameter $n = 3$ see [70]. In the case of $L(F) = F$, the effective potential takes the form of those governing photon motion in the RN spacetimes (see [76–78]).

The local minimum of the effective potential corresponds to the photon circular orbits. The radius and impact parameter of these circular orbits can be found by setting on the effective potential the condition $V'_{\rm eff} = 0$ where the prime $'$ denotes differentiation with respect to the radial coordinate. Notice that the photon circular orbits in this case govern also the quasinormal modes of electromagnetic perturbations in the Maxwellian NED RBH spacetimes [73], representing thus a special case when the quasinormal modes are not related to the null geodesics of the spacetime, first discussed in [79].

Figure 8 illustrates the dependence of the radius of circular photon orbits on the charge of the RBH, Q, for fixed values of n. It can be seen that for distances very close to the coordinate origin $r = 0$, the radius increases and then decreases as Q and n are increased.

From the viewpoint of astrophysics, more important is the impact parameter of the photon circular orbit, as it governs the size of the RBH shadow. The expression of the impact parameter takes the form [63,70,71]

$$b_c^2 = \left.\frac{L_{\rm F}}{L_{\rm F}+2FL_{\rm FF}}\frac{r^2}{f}\right|_{r=r_{\rm ph}}. \quad (23)$$

Figure 9 illustrates extension of the RBH shadow (given by the impact parameter b_c) as a function of its charge, Q, for different values of the degree parameter n. One can see

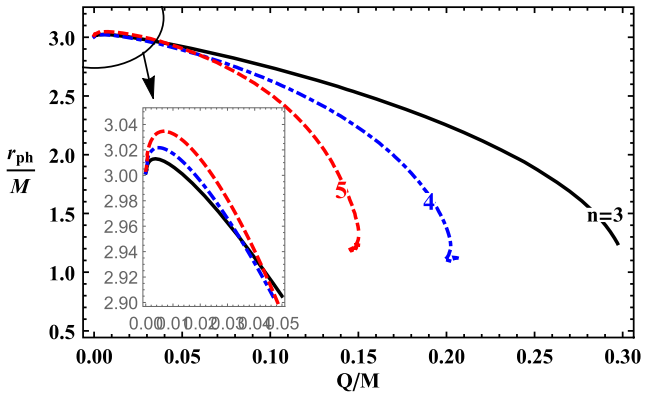

FIG. 8. The radius of photon sphere as a function of the RBH charge Q, for different values of the parameter n.

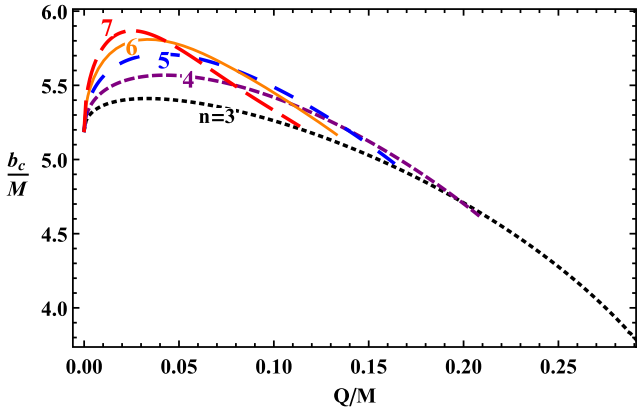

FIG. 9. The dependence of impact parameter for circular orbits of photons on the RBH charge Q, for different values of the parameter n.

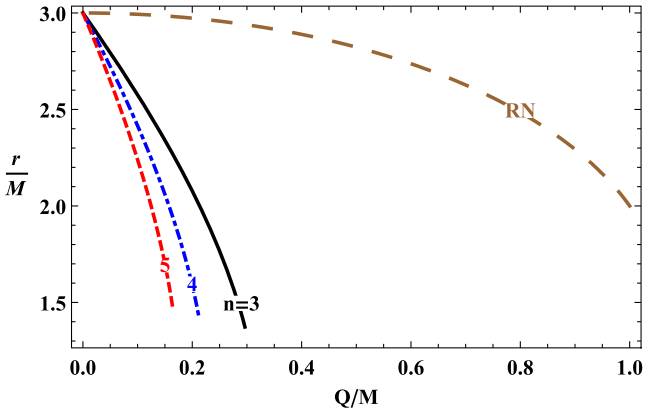

FIG. 10. Comparison of the radius of circular null geodesics of massless neutrino-like particles in the Maxwellian NED RBH spacetimes with different values of n. The results are compared to those corresponding to the RNBHs.

that the effect of the parameters Q and n on the impact parameter are similar to photon sphere. In small values of Q the effect of n dominates and the value of the impact parameter increases as increases n, while with increasing value of Q effect of n decreases and at the same time the value of the impact parameter also decreases, then effect of Q dominates. One can notice that the value of b_c in the case $n \geq 4$ at $Q_{\rm ext}$ equals to the value of b_c in case $n = 3$ at $Q = Q_{\rm ext}^{n\geq 4}$.

B. The motion of neutrinolike particles

Calculating the equations of motion for massless ("neutrinolike") particles is simpler than the photon case. One can use again the standard Euler-Lagrange equations utilizing the metric given by the lapse function with Eq. (3).

Considering the dimensionless Lagrangian density for a neutral particle with mass m

$$L_{\rm p} = \frac{1}{2} g_{\mu\nu} \dot{x}^{\mu} \dot{x}^{\nu}, \tag{24}$$

the conserved quantities of motion read

$$p_t = \frac{\partial L_{\rm p}}{\partial \dot{t}} \Rightarrow g_{tt}\dot{t} = -\mathcal{E} \tag{25}$$

$$p_\phi = \frac{\partial L_p}{\partial \dot{\phi}} \Rightarrow g_{\phi\phi}\dot{\phi} = \mathcal{L} \tag{26}$$

where $\mathcal{E}$ and $\mathcal{L}$ are the special energy and angular momentum of the particle, respectively. Equations of motion for a test particle in the equatorial plane are then governed by the normalization condition

$$g_{\mu\nu} u^{\mu} u^{\nu} = \epsilon \tag{27}$$

where ϵ is 0 and -1 for massless and massive particles, respectively.

Taking into account Eqs. (25)–(26) we can introduce the effective potential for massless particles ($\epsilon = 0$) considering

$$\frac{\dot{r}^2}{\mathcal{L}^2} + V_{\rm eff} = \frac{\mathcal{E}^2}{\mathcal{L}^2},$$

and we obtain

$$V_{\rm eff} = \frac{f}{r^2}. \tag{28}$$

Circular orbits for massless particle can be found in the standard way by setting condition $V'_{\rm eff} = 0$ which implies

$$f' - \frac{2}{r} f = 0 \tag{29}$$

while for the impact parameter of the circular null geodesics of the spacetime itself, we have simple relation [70]

$$b^2_{c({\rm neu})} = \left.\frac{r^2}{f}\right|_{r=r_{\rm neu}}. \tag{30}$$

The analytical solution of Eq. (29) is rather complex, we thus present the results of the numerical solution for the circular orbits of massless particles in Fig. 10, providing the dependence of radius of the circular orbits for on the RBH charge Q for different values of the nonlinearity degree parameter n. We can see that the radius of the circular orbit decreases as the parameters Q and n are increased. The rate of decrease is inversely proportional to the parameter n. The decrease is always faster for RBHs than for the RNBHs.

IV. THE MOTION OF TEST PARTICLES

For the massive electrically uncharged particles the motion is governed by timelike geodesics of the spacetime,

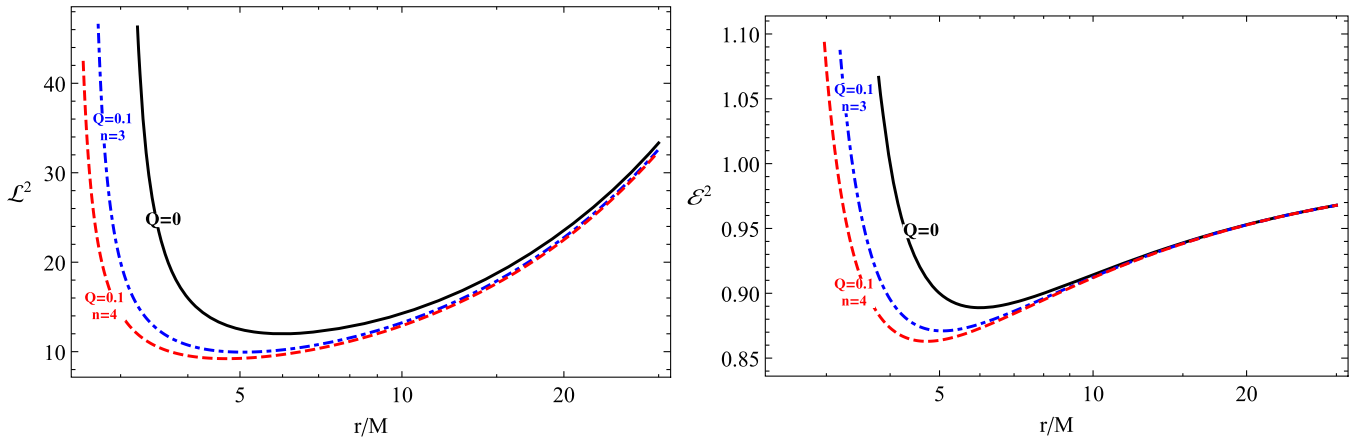

FIG. 11. Radial profiles of the specific angular momentum (at the left panel) and specific energy (at the right one) of neutral particles in circular orbits, given for characteristic values of RBH charge, Q, and the degree, n.

and the equations of motion can be found by using Eq. (27). Taking into consideration Eqs. (25) and (26), we obtain the motion equations in the separated and integrated form

$$\dot{r}^2 = \mathcal{E}^2 + g_{tt}\left(1 + \frac{\mathcal{K}}{r^2}\right) \tag{31}$$

$$\dot{\theta} = \frac{1}{g_{\theta\theta}^2}\left(\mathcal{K} - \frac{\mathcal{L}^2}{\sin^2\theta}\right) \tag{32}$$

$$\dot{\phi} = \frac{\mathcal{L}}{g_{\phi\phi}} \tag{33}$$

$$\dot{t} = -\frac{\mathcal{E}}{g_{tt}} \tag{34}$$

where $\mathcal{K}$ denotes the Carter constant corresponding to the total angular momentum.

Restricting the motion of the particle to the equatorial plane, in which $\theta = \pi/2$ and $\dot{\theta} = 0$, the Carter constant takes the form $\mathcal{K} = \mathcal{L}^2$ and the equation of the radial motion can be expressed in the form

$$\dot{r}^2 = \mathcal{E}^2 - V_{\text{eff}} \tag{35}$$

where the effective potential of the motion of neutral particles reads

$$V_{\text{eff}} = f\left(1 + \frac{\mathcal{L}^2}{r^2}\right). \tag{36}$$

In order to derive the motion constants of circular motion of a neutral particle at a radius r, we apply the standard conditions for the circular motion, meaning no radial motion ($\dot{r} = 0$) and no forces in the radial direction ($\ddot{r} = 0$). We obtain for the neutral particle motion in the field of NED RBHs governed by the lapse function in Eq. (4) the radial profiles of the specific angular momentum and specific energy for circular orbits in the following form

$$\mathcal{L}^2 = \frac{Mr[1 + (1-n)\frac{Q}{r}]}{(1+\frac{Q}{r})^{n+1} - [3 + (3-n)\frac{Q}{r}]\frac{M}{r}}, \tag{37}$$

$$\mathcal{E}^2 = \frac{(1+\frac{Q}{r})^{1-n}[(1+\frac{Q}{r})^n - \frac{2M}{r}]^2}{(1+\frac{Q}{r})^{n+1} - [3 + (3-n)\frac{Q}{r}]\frac{M}{r}}. \tag{38}$$

The radial profiles of the specific angular momentum $\mathcal{L}(r; M, Q, n)$ and specific energy $\mathcal{E}(r; M, Q, n)$ of the circular motion, given by Eqs. (37) and (38) are determined by the parameters of the RBH Q and n and fix the values of these motion constants at any given radius r. We are giving the squares of the motion constants as in the spherically symmetric spacetimes the corotating orbits are equivalent to counterrotating ones.

Figure 11 illustrates the radial profiles of the specific angular momentum and the specific energy of the neutral particle circular orbits, constructed for characteristic values of the RBH parameters, Q and n, and compared to the Schwarzschild BH case having $Q = 0$. We can see that both the radial profiles of the specific angular momentum and the specific energy are decreasing with increasing RBH parameters n and Q. Note that in the decreasing part of the radial profiles, the circular orbits are stable against the radial perturbations, while in the increasing part, the circular orbits are unstable [80]. The minimum of the profiles corresponds to the so-called marginally stable, or innermost stable circular orbit (ISCO) that is related to the inflexion point of the effective potential. The specific energy of the ISCO orbit determines efficiency of the Keplerian accretion following the stable circular geodesics [81]—with the specific energy of the ISCO decreasing, efficiency of the accretion is increasing. We thus see that the efficiency of the Keplerian accretion increases with increasing parameters Q and n.

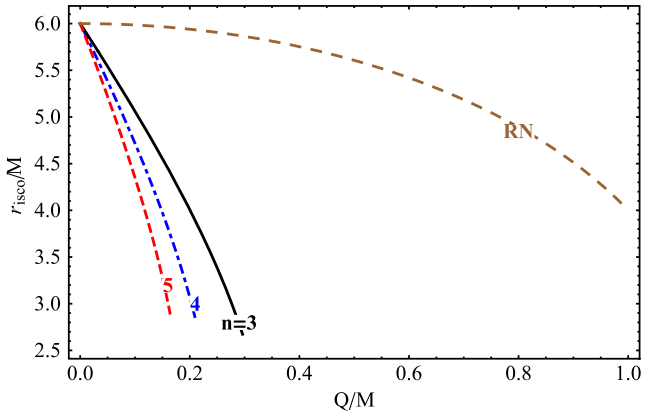

FIG. 12. The ISCO radius for neutral particle motion in the field of the NED RBHs, given in dependence on parameter Q for characteristic values of n. For comparison the dependence of ISCO on Q is given for RNBHs.

There is another important circular geodesic orbit, namely the marginally bound orbit (MBO) with specific energy $E = 1$ that is unstable against the radial perturbations—this orbit represents a natural limit on the so called thick accretion disks from perfect fluid where the structure is governed also by the fluid pressure [82,83].[2] We thus now consider these limiting orbits, ISCO and MBO, in the Maxwellian NED RBH spacetimes.

A. Innermost stable circular orbits (ISCO)

Circular orbits of massive neutral particles are stable if the condition $V''_{\rm eff} \geq 0$ is satisfied, and unstable for the condition $V''_{\rm eff} < 0$; the ISCO is determined by the condition $V''_{\rm eff} = 0$. The ISCO radius is determined as solution of the equation

$$\frac{2M}{r}\left[3-3(n-2)\frac{Q}{r}-(n-3)(n-1)\frac{Q^2}{r^2}\right] - \left(1+\frac{Q}{r}\right)^n\left[1+(n+2)\frac{Q}{r}-(n^2-1)\frac{Q^2}{r^2}\right]\geq 0. \quad (39)$$

We study the ISCO radius $r_{\rm ISCO}$ for neutral particles by numerical solution of Eq. (39). Figure 12 shows the dependence of the ISCO radius for neutral particle motion around Maxwellian NED RBH spacetimes in dependence on their electrical charge Q for fixed values of the degree parameter n. The ISCO radius decreases with increasing charge parameter, and the rate of decrease of the ISCO radius increases with increasing n being always larger for RBH than for RNBHs.

[2]In the BH spacetimes reflecting the cosmic repulsion (cosmological constant) the definition of the MBO is more complex [4,84,85]

TABLE I. Numerical values of $\mathcal{E}_{\rm ISCO}$ for the different values of the RBH parameters Q and n.

	$Q = 0.1$	$Q = 0.15$	$Q_{\rm max}$
$n = 3$	0.8710	0.8588	0.7844
$n = 4$	0.8629	0.8418	0.7932
$n = 5$	0.8532	0.8156	0.7976

B. Energy efficiency of Keplerian accretion

It is well known that efficiency of the Keplerian accretion in geometrically thin disks, governed by the properties of the spacetime circular geodesics, is determined by the specific energy of the innermost (marginally) stable circular geodesic (ISCO) [81]. The efficiency is given by the relation

$$\eta = 1 - \mathcal{E}_{\rm ISCO}, \quad (40)$$

where $\mathcal{E}_{\rm ISCO}$ is the dimensionless (normalized to the rest energy of test particle mc^2) energy of the test particle at the ISCO. The efficiency represents maximum energy that can be extracted and converted into radiation from the rest energy of the falling matter in the process of Keplerian accretion. The specific energy $\mathcal{E}_{\rm ISCO}$ governing the Keplerian accretion can be obtained by using Eq. (38) at $r = r_{\rm ISCO}$. We give $\mathcal{E}_{\rm ISCO}$ for several characteristic values of the RBH parameters Q and n in Table I.

One can see from the Table that the energy $\mathcal{E}_{\rm ISCO}$ decreases (the efficiency increases) with increasing values of the RBH parameters Q and n. However, in the case of extremely charged RBH (with $Q = Q_{\rm max}$) the specific energy $\mathcal{E}_{\rm ISCO}$ slightly decreases with increasing the value of the parameter n.

C. Marginally bound orbits of neutral particles

Massive particles on the marginally bound orbits (MBO) have their energy equal to the rest energy, $\mathcal{E} = 1$, thus their binding energy is equal to zero. The radius of the MBO can be given due to Eq. (38) by the relation

$$1 - \frac{4M}{r}\left(1+\frac{Q}{r}\right)^{1-n} + (1+n)\frac{Q}{r} = 0 \quad (41)$$

Here we give the MBO for fixed values of the degree n. The solution for $n = 3$ reads

$$3r_{\rm mb} = 4M - 6Q + R(M,Q) + \frac{16M^2 - 48MQ + 9Q^2}{R(M,Q)} \quad (42)$$

where

$$R^3(M,Q) = 64M^3 - 288M^2Q + 270MQ^2 - 27Q^3 + 6\sqrt{3MQ^3(207MQ - 64M^2 - 27Q^2)};$$

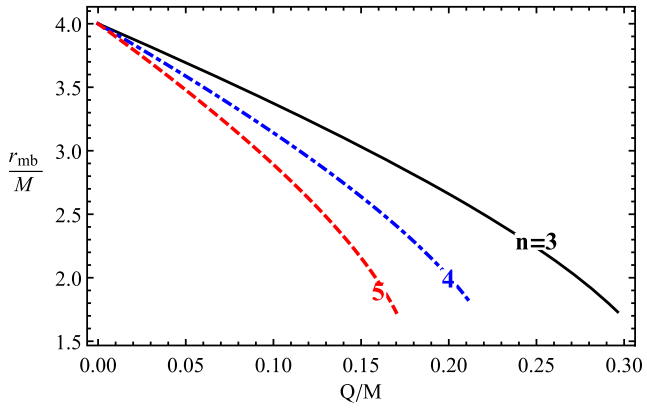

FIG. 13. The radius of marginally bounded orbits as a function of the RBH charge Q, for the different values of the degree of nonlinearity n.

in the Schwarzschild case $Q = 0$, $R = 2M$ and $r_{mb} = 4M$. For $n \geq 4$, Eq. (42) is a bit longer and more complicated. For this reason, we determine the solutions numerically and represent them graphically in Fig. 13. The radii of the MBOs are given as a functions of the RBH charge Q for typical values of n. One can see that the radius decreases as both the values of Q and n increase. The minimum values of r_{mb} comes closer to the event horizon as $Q^{(n)} \to Q^{(n)}_{ext}$.

V. CHARGED PARTICLE MOTION

In this section we study the motion of a charged particle with mass m and electric charge e in the combined gravitational and electromagnetic fields determined by the lapse function of Eq. (4) and the electromagnetic vector four-potential given by Eq. (5).

A. Equations of motion for charged particles

Motion of charged test particles in charged backgrounds is governed by the Lorentz equation

$$u^\mu \nabla_\mu u^\nu = q F^\nu_\sigma u^\sigma. \tag{43}$$

We use the specific charge $q = e/m$. The Lorentz equation can be related to the Euler-Lagrange method. The Lagrangian for a charged particle motion in a gravitational field combined with an electromagnetic field reads

$$L_{ch\,p} = \frac{1}{2} g_{\mu\nu} \dot{x}^\mu \dot{x}^\nu + q A_\mu \dot{x}^\mu \tag{44}$$

where A_μ are the components of the electromagnetic four-potential given by Eq. (5). The motion constants determined by the stationarity and axial symmetry of the background are given by the relations

$$g_{tt}\dot{t} + q A_t = -\mathcal{E} \tag{45}$$

$$g_{\phi\phi}\dot{\phi} = \mathcal{L} \tag{46}$$

where $\mathcal{E}$ represents the specific energy and $\mathcal{L}$ represents the specific axial angular momentum of the particle, respectively, related to observers at rest at $r \to \infty$. Due to the spherical symmetry of the background we can make simplification and consider only the equatorial motion (at fixed $\theta = \pi/2 = \text{const}$) and the Euler-Lagrange method again enables introduction of an effective potential.

The effective potential for a charged particle in the equatorial plane ($\theta = \pi/2$ and $\dot{\theta} = 0$) can be found by solving equation $\mathcal{E} = V_{eff}$ (taking $\dot{r} = 0$), taking the form

$$V^{\pm}_{eff}(r) = q A_t \pm \sqrt{f\left(1 + \frac{\mathcal{L}^2}{r^2}\right)} \tag{47}$$

In this study, we consider the positive root of the effective potential, V^{+}_{eff}, as it corresponds to the so called positive-root states with four-velocity oriented to future and positive energy relative to local observers—for details see [80,86,87].

Figure 14 demonstrates how the minimum of the effective potential, governing the circular orbits, changes for various charged particles. The angular momentum, $\mathcal{L} = 4.3M$, around the RBH is assumed along with values for Q and n. The leftmost panel of the figure illustrates that the minimum of the effective potential, as the charge of the RBH increases, reacts chaotically for $n = 3$, while the middle panel shows that the minimum shifts upward for

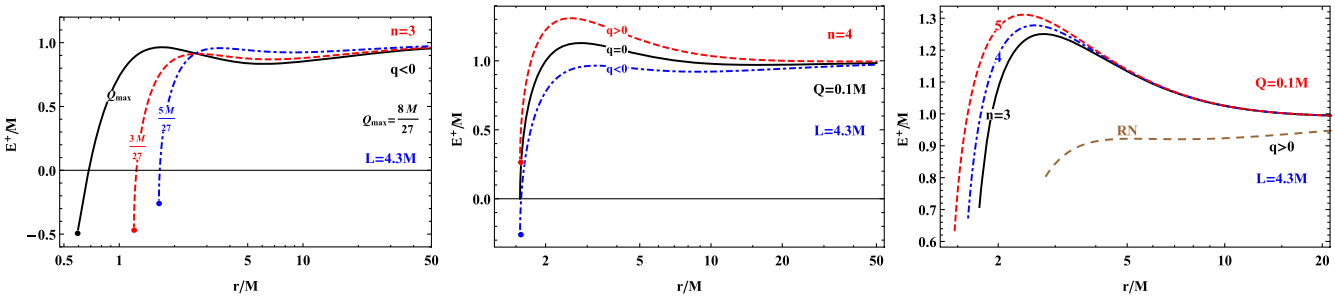

FIG. 14. The effective potential for fixed specific axial angular momentum and charged particles with various specific charge moving around a RBH with different values of Q and n.

positive charges and downward for negative charges for $n = 4$, as related to the effective potential for uncharged particles. The rightmost panel is slightly different as it illustrates the minimum for the positive charges $q > 0$ of varying degrees of nonlinearity $n = 3, 4, 5$. It is seen that as n increases the minimum Coulomb potential decreases and the maximum of the effective potential increases and shifts to the center. Also shown in the same panel is effective potential curve for a RNBH, and how it differs from the RBH case for similarly charged particle. The minima of the effective potential govern again the stable circular orbits of charged particles, while the maxima correspond to the unstable circular orbits. The circular orbits of charged test particles around RNBHs were studied in [52,80,86].

B. Circular orbits and the ISCO

Stable circular orbits in the equatorial plane can be studied using the following standard conditions

$$V_{\rm eff} = \mathcal{E}, \qquad V'_{\rm eff} = 0, \qquad V''_{\rm eff} \geq 0. \tag{48}$$

The solutions of the equation $V'_{\rm eff} = 0$ in the fixed background imply that the particle with given specific charge q follows a circular orbit at a given radius r, if its specific angular momentum is given by the relation

$$\mathcal{L}^2_{\pm} = \frac{1}{(rf' - 2f)^2}\left[2r^3 f(q^2 r A'^2_t + f') - r^4 f'^2 \pm 2qr^3 f A'_t \sqrt{q^2 r^2 A'^2_t - 2(rf' - 2f)}\right] \tag{49}$$

The prime, $'$, on $V'_{\rm eff}$ or other quantities denotes the partial derivative with respect to the radial coordinate. In the case when $Q = 0$ (i.e., the Schwarzschild case) the angular momentum solutions for circular orbits from above takes the form

$$\mathcal{L}^2_{\pm} = \frac{Mr^2}{r - 3M}.$$

We now analyse the solution (49) looking for the condition where both $\mathcal{L}^2_{\pm}$ are real.

In order to ensure that we obtain a real solution to Eq. (49), we require that the function under the square root is always positive,

$$(qrA'_t)^2 - 2(rf' - 2f) \geq 0. \tag{50}$$

Therefore, in regards to the specific angular momentum at the circular orbit we must consider two cases:

(1) since $(qrA'_t)^2$ is always positive, then $rf' - 2f \leq 0$ must be searched for any specific charge q and for $q = 0$
(2) when $rf' - 2f > 0$ then $(qrA'_t)^2 \geq 2|2f - rf'|$ must be satisfied for large values of particle's charge

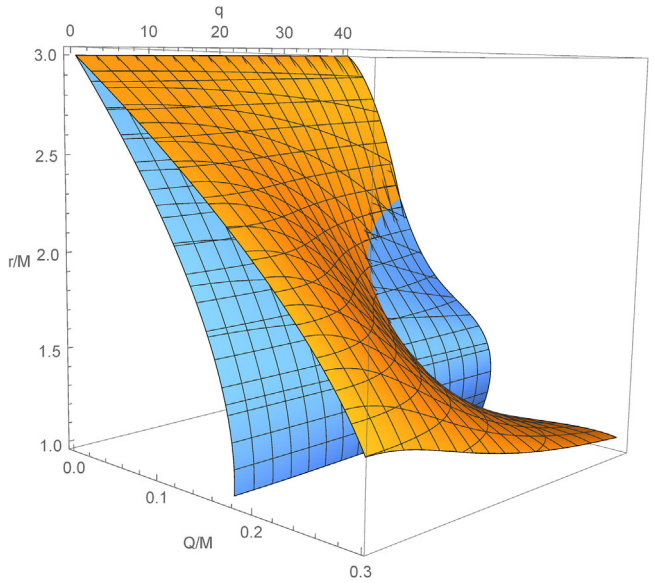

FIG. 15. The zeros of the left side in relation (49) governing the critical surfaces of the parameter space determining regions allowing of circular orbits. The orange 3D surface is relevant for $n = 3$, and the blue one for $n = 5$. The regions to the "right" or "above" either surface corresponds to the values of r, Q, and q for which the specific angular momentum is real-valued for the given value of n.

We rewrite the condition (50) in the form

$$\frac{q^2Q^2}{(1+\frac{Q}{r})^{2n}}\left[1 - 3(n-2)\frac{Q}{r} + (n-3)(n-1)\frac{Q^2}{r^2}\right]^2 + 4r^2\left(1+\frac{Q}{r}\right)^{3-n}\frac{M}{r}\left[3 - (n-3)\frac{Q}{r}\right] \geq 0. \tag{51}$$

The condition (51) can be satisfied simultaneously by looking at the 3D "surface" in Fig. 15 formed by considering the variables q, Q, and r and assuming a fixed value for n. It is illustrated that in dependence on the charge of the RBH, Q, and the particle specific charge q, a critical distance $r_{\rm crit}$ from the RBH is defined where the circular orbits are allowed. For the orange surface, $n = 3$, and the blue surface, $n = 5$ the distance decreases as Q is increased. The figure also illustrates that when $Q = 0$, the particle is at distance $r_{\rm crit} = 3M$, as expected in the Schwarzschild case.

At large values of Q and q, the critical distance depends on both the black hole charge Q and the particle charge q. Clearly since $\mathcal{L}^2$ is always positive the critical distance $r_{\rm crit} < r$, and the region above the surface corresponds to the appropriate values of r, Q, and q that satisfy the real-valued angular momentum found in (49).

One can also see from Fig. 15 that the critical radius, $r_{\rm crit}$, decreases for neutral particles as well as for charged particles of smaller charge around a RBH of increasingly higher charge, Q. The rate at which this distance decreases becomes larger as n increases. This corresponds to a value

of the critical distance where $r_{\rm crit}^{n=3} > r_{\rm crit}^{n=5}$ for a given Q. However, for large values of q (it is approximately at $q \gtrsim 10$) the decreasing rate decreases with increasing n and the surface corresponding to $n = 3$ intersects with the blue surface corresponding to $n = 5$. Where the two surfaces intersect indicates where the critical distance is the same for degrees of nonlinearity $n = 3$ and $n = 5$. Within the region bounded by these two surfaces, $r_{\rm crit}^{n=3} < r_{\rm crit}^{n=5}$ for values of $Q^n \to Q_{\rm max}^n$.

One can see from Eq. (49) that $\mathcal{L}_+^2 < \mathcal{L}_-^2$ for positive charges and $\mathcal{L}_-^2 > \mathcal{L}_+^2$ for negatively charged particles. Therefore $\mathcal{L}_+^2|_{q<0} = \mathcal{L}_-^2|_{q>0} < \mathcal{L}_+^2|_{q>0} = \mathcal{L}_-^2|_{q<0}$.

Since the conditions in (48) were required in order to have stable circular orbits, they imply that no forces acting on the charged particle competing against each other. Yet, there are three forces on the particle while it is in the orbit around the RBH: the Coulomb (C), gravitational (G), and centrifugal (Cf) forces. For negatively charged particle the G and C forces point in the same direction and Cf points into the RBH. Under the condition that the sum of the C and G forces balance out the Cf force, which means that for negatively charged particles we use $\mathcal{L}_-^2$, since Cf is proportional to $\mathcal{L}^2$ and the value of the $\mathcal{L}^2$ should be large enough in order to ensure that the particle does not fall into the central object. This means that for positively charged particles the Cf and C forces the same direction and we can only use for positively charged particle also $\mathcal{L}_-^2$, because the value of $\mathcal{L}^2$ should be small enough, otherwise, the particle will be pulled away to infinity. Using these facts, we analyze the radii of the circular orbits of charged particles using the solution $\mathcal{L}_-^2$ of Eq. (49), where $r > r_{\rm crit}$.

Figure 16 shows the specific angular momentum which corresponds to the circular orbit for negatively charged particles as a function of the dimensionless radial coordinate, r/M. One can see from the panel at the top that the value of $\mathcal{L}_-^2$ increases as Q is increased for given values of the negatively charged particle q. We show the curves for the specific angular momentum for two negatively charged particles with $q = -10$ and $q = -60$. We can see from the bottom panel that for $q = -10$ increasing of the charge of the RBH causes the minimum of the function $\mathcal{L}_-^2$ to increase for differing values of Q up to the extreme charge when $n = 3$. For $q = -60$, increasing of the RBH charge results in increasing minimum value of the specific angular momentum, and the critical distance where $\mathcal{L}_-^2$ is minimized starts to increase but then decreases. One can conclude from the two panels that increasing the particle specific charge results in increasing specific angular momentum.

Figure 17 illustrates similar situation with the same RBH parameters as presented in Fig. 16, but only for positive specific charges of the particles.

Now, we can study stable circular orbits for a charged particle in the background of the Maxwellian NED RBH, determined by the condition $V''_{\rm eff} \geq 0$. The stable circular

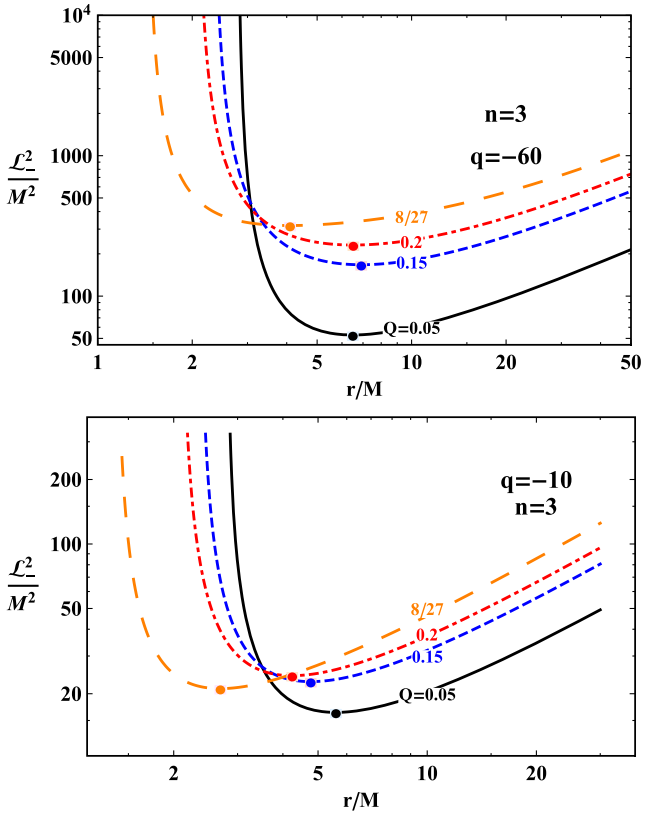

FIG. 16. Radial profiles of the square of the specific angular momentum which correspond to circular motion for different values of the RBH parameters Q, and n, and particle specific charge q.

orbits for charged particles with a given specific charge q have to be located above the ISCO radius that corresponds to the minimum of the radial profile of the specific angular momentum governing the circular orbits—see Fig. 16. Figure 18 shows the ISCO for charged particles as a function of the charge of the RBH.

The top panel profiles the ISCO radii for positively charged particles when $n = 3$. One can see that for large values of q the ISCO radii decrease reaching its minimum value, and then increase to infinity as the charge of the RBH tends to $Q = Q_{\rm crit}$; for small values of q, the ISCO radii decrease with increasing Q.

It is seen from the figure that under the condition

(i) $Q < Q_{\rm crit}$: circular orbits are allowed around the RBH.

(ii) $Q \geq Q_{\rm crit}$: the ISCO tends to infinity where there are no circular orbits around the RBH and the positively charged particle goes to infinity due to the Coulomb interaction and centrifugal forces being much larger than gravity (which is an attractive force).

Note that one can see from the panel that for positively charged particles the ISCO radius is heavily influenced by the specific charge, q, for a RBH having the critical charge, $Q_{\rm crit}$. As the specific charge of the particle q increases, the

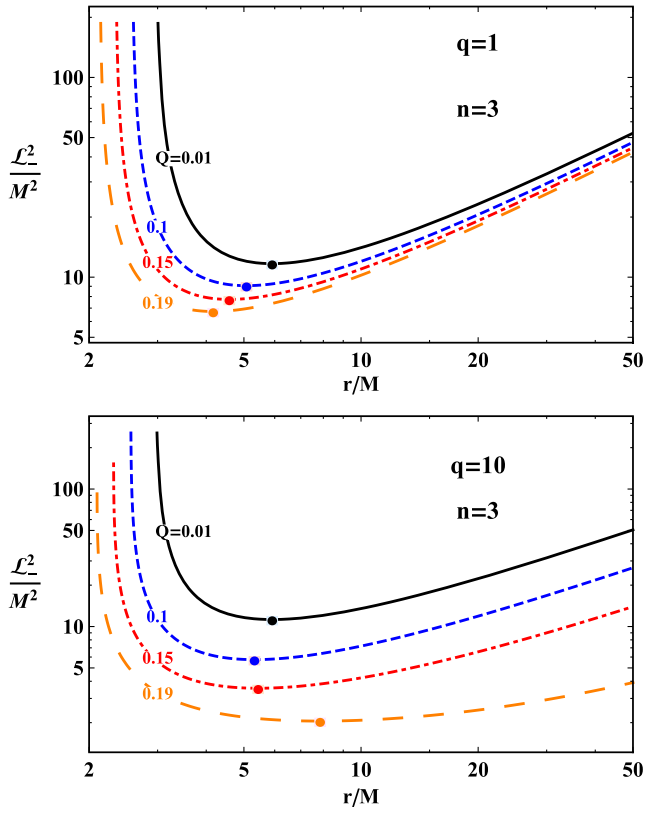

FIG. 17. The radial profiles of the specific angular momentum as in Fig. 16, but for positively charged particles.

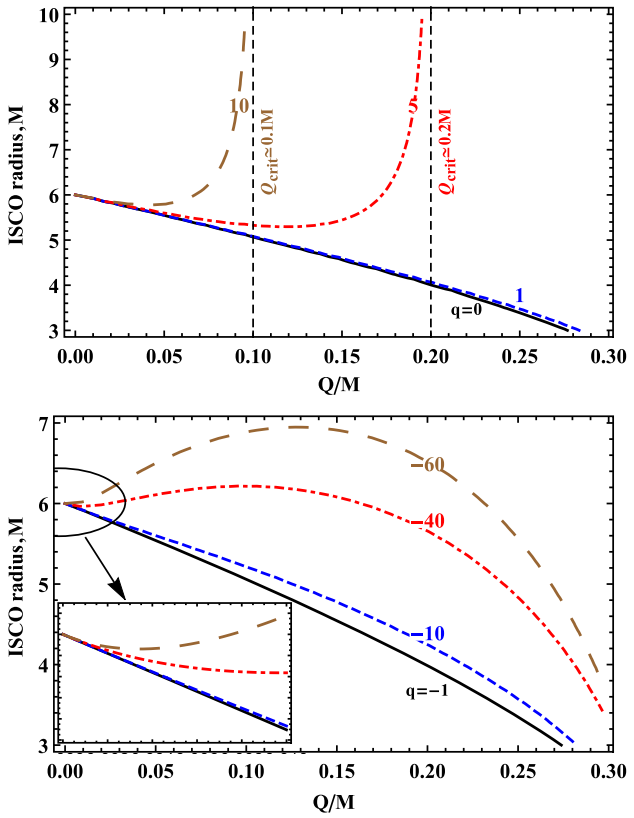

FIG. 18. The dependence of ISCO radius for negative (at the bottom panel) and positive(at the top panel) charged particles on the RBH charge, Q.

critical charge of the RBH $Q_{\rm crit}$ decreases. The bottom panel of Fig. 18 illustrates the ISCO radius for negatively charged particles when $n = 3$.

Figure 19 illustrates how the ISCO radius as a function of the charge of a RBH, for a charged particle with $q = 5$, changes while varying the degree of nonlinearity n. Notice how the ISCO curve shifts to the right as n is increased, while the asymptotic RBH charge $Q_{\rm crit} = 0.2M$ from Fig. 18 is the same for all n. When $Q > Q_{\rm crit}$, the Coulomb interaction dominates and this region illustrates where the particle orbits are no longer stable.

Moreover, we can see from Figs. 18 and 19 that the ISCO radius is $r_{\rm ISCO} = 6M$ at two points: when $q = Q = 0$ and $q \neq 0$ and $Q \neq 0$. Here we are interested in the cases what the values of q and Q must be in order for the ISCO radius to be the same as the ISCO for a particle around Schwarzschild BH ($r_{\rm ISCO} = 6M$).

Figure 20 shows how the ISCO radius varies as a function of the RBH charge for various values of the degree of nonlinearity. As n increases, the maximum of the ISCO radius decreases and the corresponding charge Q also decreases. Notice that there are two different RBH of some charge, Q, that have an ISCO radius of $r_{\rm ISCO} = 6M$ for a single particle of charge, $q = -60$.

Figure 21 illustrates the relation between the particle charge and the ISCO of the particle while varying the RBH charge and the nonlinearity degree n. We can see that the ISCO radius decreases as n and Q are increased. Notice that because the ISCO curves intersect for two oppositely charged particles there can are two different particles that have the same ISCO radius for two differently parametrized RBHs.

In Fig. 22 we consider how charged particles and the charge of the RBH relate to the ISCO radius at the distances

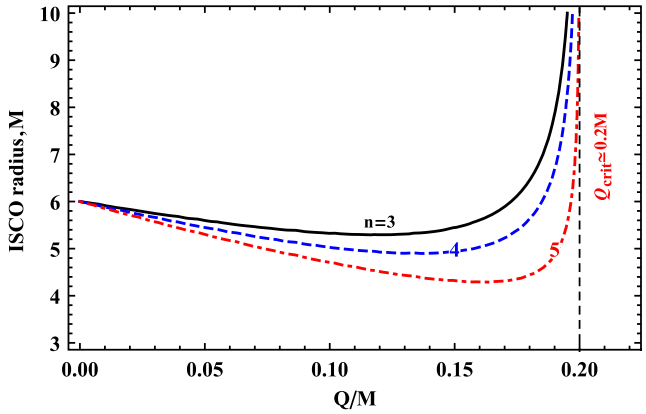

FIG. 19. The ISCO radius of positively charged particles with value $q = 5$ for different values of n.

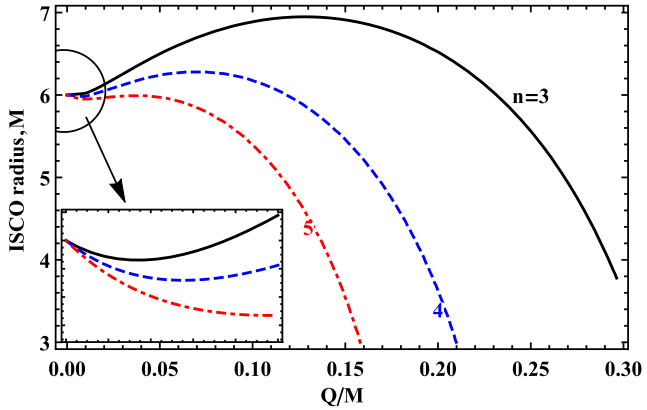

FIG. 20. The ISCO radius for the particle from Fig. 18 of charge, $q = -60$, for different values of $n = 3, 4, 5$.

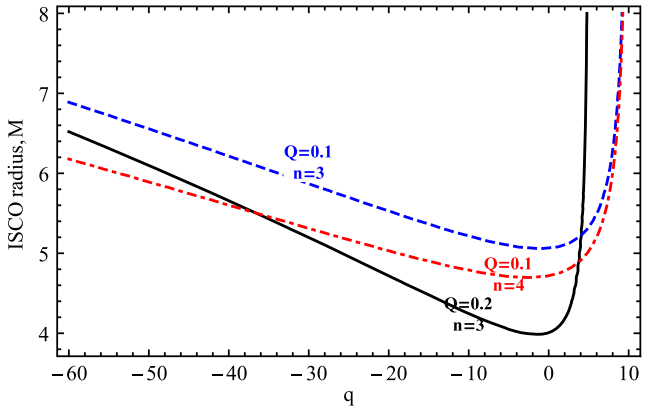

FIG. 21. ISCO radius for charged particles as a function the particle charge q for different values of the RBH charge Q and the degree n.

around $r = 6M$. Recall that, in general, the ISCO radius exists for strongly bounded particles where $Q < Q_{\text{crit}}$. One can see in this figure that as the degree of nonlinearity increases, the ISCO radius is preserved for large values of q and small values of Q. The colored regions illustrate that, for fixed $n = 3$, for certain values of q and Q the ISCO radius is smaller than $6M$.

The border of the white region and colored regions indicates when the ISCO is equal to $6M$. The values of q and Q that lie on this line correlates to the ISCO for a particle around a Schwarzschild BH. This means that a particles with charge q around a RBH of charge Q can be observed to have an ISCO radius of $6M$. Below we illustrate how Q and q relate to profile different values of the ISCO radius for charged particles.

Figure 23 illustrates how Q and q relate to give certain values for the ISCO radius when $n = 3$. It is shown that for positive charges there is only a single RBH for which a particular particle can have a given ISCO radius, but in the case of negatively charged particles the opposite is true,

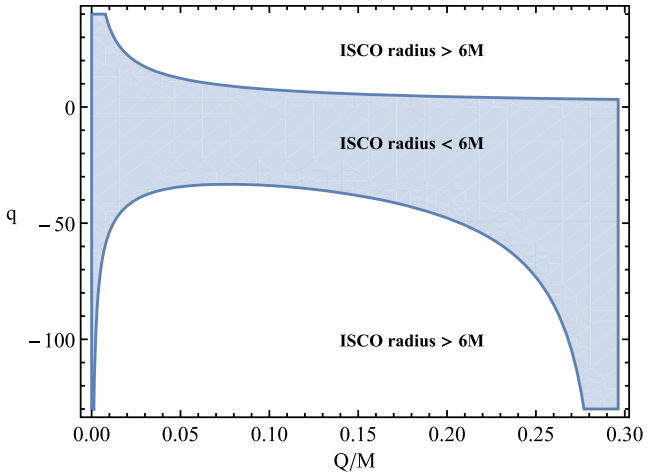

FIG. 22. Above is a contour plot relating Q and q where their corresponding ISCO radius is larger or smaller than the Schwarzschild radius for $n = 3$.

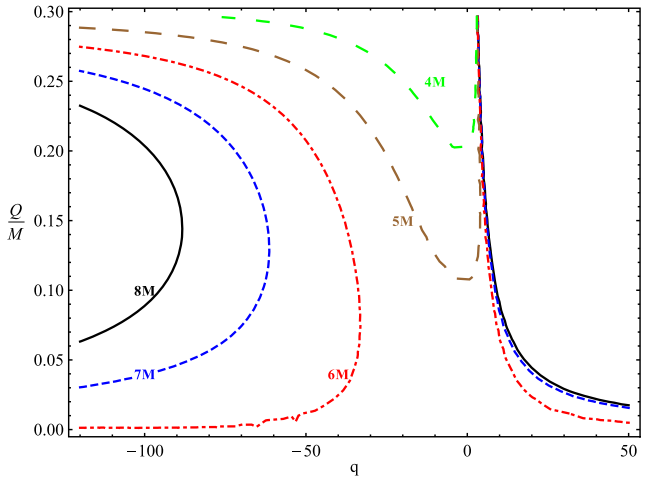

FIG. 23. Q and q profile for different values of the ISCO, for $n = 3$.

indicating that there can be two differently charged RBHs for a single negatively charged particle.

C. Marginally bound orbits of charged particles

As we mentioned in Sec. IV C, the specific energy of a charged particle following the MBO is equal to its rest energy. The energy of charged particles following the circular orbits can be given in the form

$$\mathcal{E} = qA_t + \sqrt{f\left(1 + \frac{\mathcal{L}^2}{r^2}\right)}. \tag{52}$$

The condition $\mathcal{E} = 1$ implies a relation for the specific angular momentum of the particles following the MBO that should be compared to the radial profiles of the specific

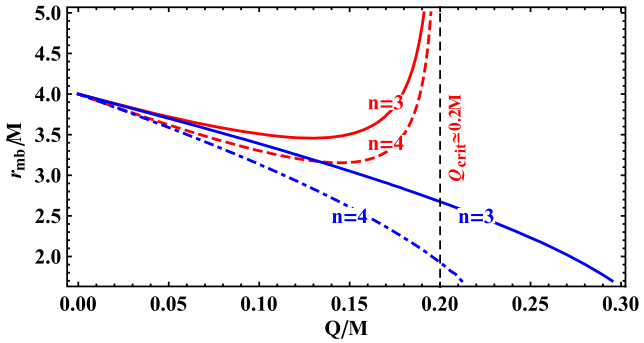

FIG. 24. The radius of marginally bound orbits for charged particles as a function of the RBH charge for negative (blue line) and positive (red line) charged particles of charge, $q = 5$.

angular momentum of circular orbits, and the radius of MBO can be determined easily by numerical methods.

Below we present an illustrative example of the study of the positions of the MBO as function of RBH charge Q for fixed values of $n = 3$ and $n = 4$, and positively and negatively charged particles.

In Fig. 24 we have demonstrated the dependence of the radius of the MBOs on the RBH charge parameter for the different values of the parameter of nonlinearity n. One can see that for the critical value $Q_{\rm crit} = 0.2$ the MBOs of positively charged particles goes to infinity at $qQ_{\rm crit} \simeq 1$. The marginally bounded orbits for negatively charged particles become smaller as Q and n are increased.

D. Trajectories of particles around RBH

In order to illustrate explicitly the role of the Coulomb electromagnetic interaction of charged particles and charged RBHs, we present a simple example of trajectory of an uncharged particle in comparison to trajectories of positively and negatively charged particles.

Figure 25 shows trajectories of neutral ($q = 0$) and charged particles with specific charges $q = 1, q = -1$, having similar initial conditions. We assume that all the particles have the same specific angular momentum $\mathcal{L} = 3.15$ that remains constant during their motion. For all the particles, we assume the starting point at a turning point of their motion located at the coordinates $r_0 = 5$ and $\theta_0 = 1.6$. Then the neutral particle must have the specific energy $\mathcal{E} = 0.94$, while the charged particle with $q = -1$ has $\mathcal{E} = 0.92$, and those with $q = 1$ has $\mathcal{E} = 0.96$. During the motion the specific energy of each particle remains

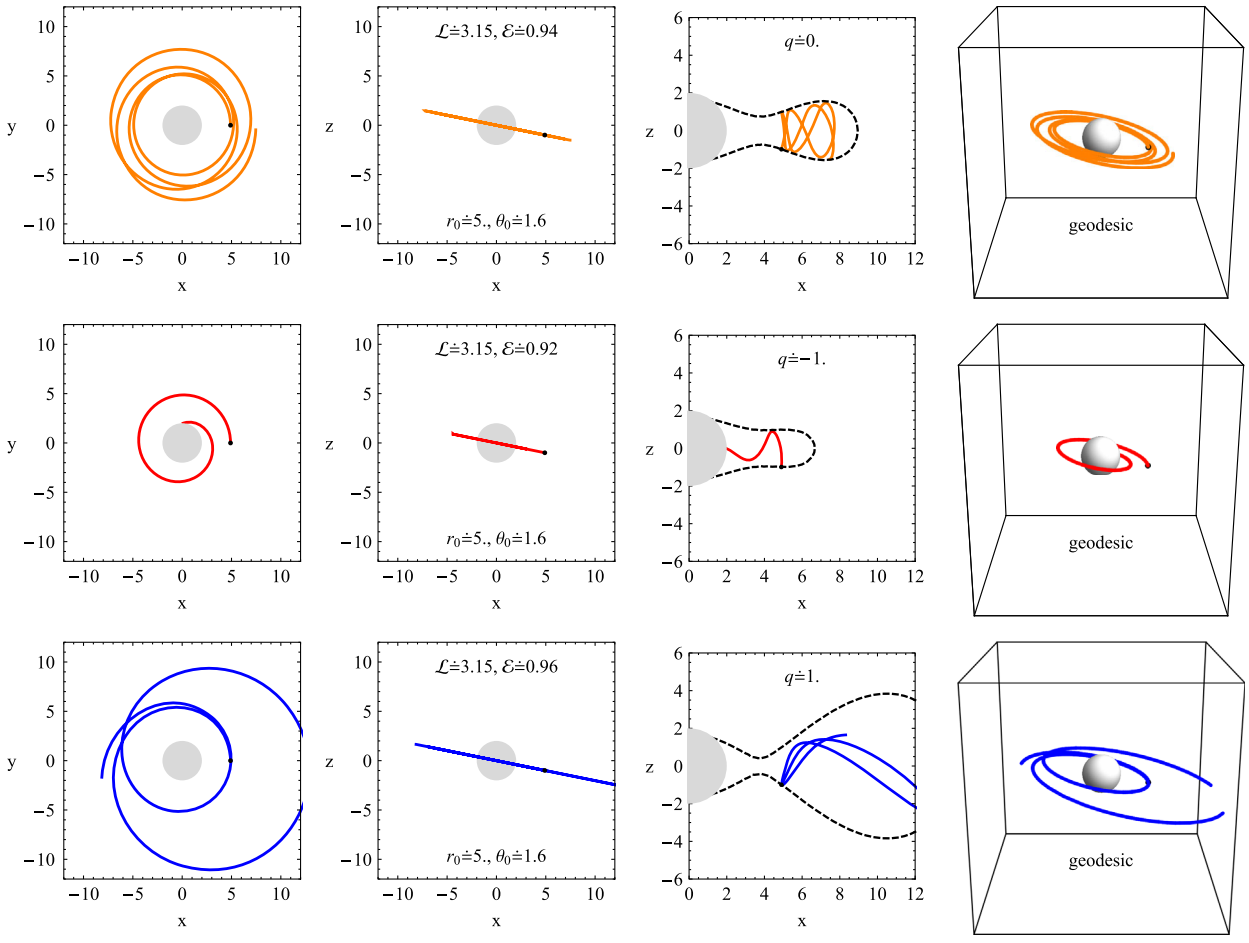

FIG. 25. Trajectories of test particles around the RBH with parameters $Q = 0.1$ and $n = 3$.

constant. We can immediately see that the neutral particle follows a bound trajectory of epicyclic motion—for the $q = -1$ particle the attractive Coulomb interaction causes in-fall of the particle into the black hole, while for the $q = 1$ particle the repulsive Coulomb interaction causes extension of the bound epicyclic motion to larger distances from the RBH. These effects are the result of the interplay of the gravitational, centrifugal and Coulomb forces.

VI. ASTROPHYSICAL APPLICATIONS

In this section we apply our studies of the photon sphere and test particle orbits around NED RBH to the real astrophysical evidence from observational data. We test how the parameters of electrically charged BHs in LED and NED can mimic the rotation parameter of Kerr BHs in relation to the photon circular orbits and the ISCO orbits, and give constrains on the parameters of the central BHs located in the well known objects Sgr A^* and M87. Here we have normalized radius and the BH parameters such as spin, electric charge to the BH mass M.

A. Photon circular orbits

First, we compare the radius of the photon circular orbit around the charged BHs with the radius of the equatorial circular photon orbit around the Kerr BHs that is determined by the expression [88]

$$r_{\rm ph} = 2\left[1 + \cos\left(\frac{2}{3}\arccos(-a)\right)\right] \tag{53}$$

Figure 26 shows the mimicker values of the BH charge corresponding to the rotation parameter of the Kerr BHs. One can see that the RN BH charge can mimic the rotation parameter up to $a = \sqrt{2}/2$. However, the considered RBHs can mimic the rotation parameter up to $a_3 = 0.966334$, $a_4 = 0.965531$ and $a_5 = 0.9073$, for $n = 3$, 4, 5, respectively.

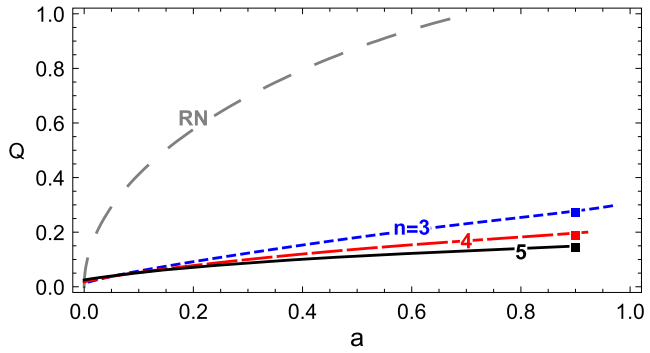

FIG. 26. Relations between BH charge and rotation parameters for the cases RN BH (brown colored, large dashed line) and RBH (blue dashed line for $n = 3$, red dashed one for $n = 4$ and black line for the case $n = 5$). The colored rectangular dots give the mimicker values of the RBH charge the rotation parameter of the BH M87 $a = 0.9$.

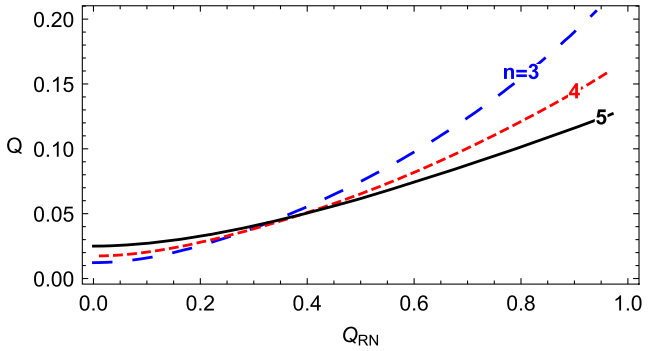

FIG. 27. Relations between RN BH charge and the charge parameter Q of the RBH giving the same radius of the photon circular orbits.

In Fig. 27 we have presented the relation between charges of the RBH and RN BH. One can see that the RN BH charge can mimic the RBH charge up to $a = 0.2$ for $Q_{\rm RN} \lesssim 0.95$ and the nonlinearity parameter $n = 3$. The upper limit of the mimicker RN BH charge slightly increases with increasing n, however, the upper value of the RBH charge parameter decreases.

1. Estimations for charge of the SM RBH M87

The theoretical analysis of observational data from the center of the Galaxy M87 shows that the rotation parameter of the central BH is about $a = 0.9 \pm 0.05$ [64] (in the Ref. [68] it is shown approximately the same $a = 0.9 \pm 0.1$). As the mimicker value of RN BH charge is much smaller than the value required by the BH spin estimated due to observations (the mimicker value of the M87 black hole charge parameter for RN BH must be $Q = 1.056$), the M87 BH cannot be considered as a purely LED charged RN BH. The mimicker values of the RBH charge for the rotation parameter of the M87 BH, obtained in [64], are given for the cases $n = 3$, 4, 5 by the relations $10^3 Q_3 = 277.56^{+3.82}_{-1.26}$, $10^3 Q_4 = 196.65^{+0.76}_{-0.78}$ and $10^3 Q_5 = 149.28^{+0.48}_{-0.57}$, respectively.

In Fig. 28 we have shown the mimicker values of the BH M87 considered as a RBH, the rotation parameter $a/M = 0.9 \pm 0.05$ (see [64]), given in $10^{-3}M$ scale. One can see the figure the mimic values of the RBH charge parameter related to the rotation parameter of the M87 BH decrease with increasing nonlinearity parameter n.

The mimicker values of the RBH charge parameter related to the rotation parameter of the M87 BH decrease with increasing nonlinearity parameter n.

B. ISCO

The stellar mass BHs are observationally relevant in microquasars, i.e., binary systems containing a BH and its

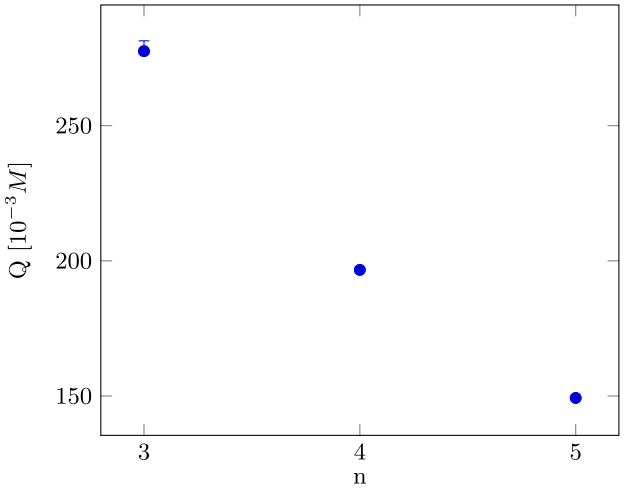

FIG. 28. Mimicker value of the charge parameter Q of the BH M87 (considering as a RBH) the measured rotation parameter in different values of the parameter n.

low mass stellar partner giving matter for the BH accretion disk whose x-ray emission is observed [65]. The BH is usually assumed to be described by the Kerr geometry—its mass parameter M is estimated by the optical observations of the dynamics of the stellar companion, while the dimensionless spin a of the black hole is estimated by the spectral fitting method [89]. The spectral fitting method is based on determination of the inner edge of the Keplerian accretion disk, i.e., on determination of the ISCO that implies the value of the spin parameter a of the Kerr geometry. However, the BH can be nonrotating and charged, being still able to give the same ISCO information as the Kerr BH—the charged BH parameters can mimic the spin parameter of the Kerr BH. As an astrophysical applications of the studies of the ISCO of neutral particles orbiting the nonrotating electrically charged BHs, we consider here the possibility to obtain the same ISCO radius for test particles following the corotating circular orbits around a Kerr BH with the dimensionless spin a, and for a NED RBH characterized by the charge parameter Q and the nonlinearity parameter n, or for the RN BH with charge Q_{RN}—such charge parameters thus mimic the spin parameter in the spectral fitting method implying necessity of additional methods in order to distinguish the Kerr BHs and the charged BH.

1. The RBH or Kerr BH?

The ISCO radius of the test particles following corotating orbits around Kerr BHs is given by the relations [88]

$$r_{\mathrm{ISCO}} = 3 + \mathrm{Z}_2 - \sqrt{(3-\mathrm{Z}_1)(3+\mathrm{Z}_1+2\mathrm{Z}_2)}, \qquad (54)$$

where

$$\mathrm{Z}_1 = 1 + (\sqrt[3]{1-a} + \sqrt[3]{1+a})\sqrt[3]{1+a^2},$$
$$\mathrm{Z}_2 = \sqrt{3a^2 + \mathrm{Z}_1^2}.$$

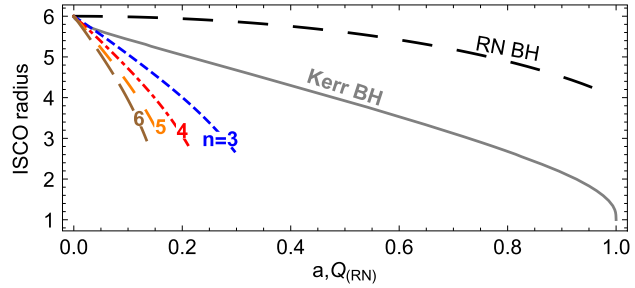

FIG. 29. ISCO radii of prograde orbits around Kerr BHs compared to the ISCO radii around NED RBHs and RN BHs.

Figure 29 illustrates the dependence of the ISCO radius of the test particles on the RBH (RN BH) charge Q and on the rotation parameter a of Kerr BHs. We can see that the effect of the rotation parameter a on the ISCO radius of the prograde orbits is much weaker than the effect of the RBH charge Q and stronger than the effect of the RN BH charge.

Relations between the RBH (RN BH) charge and rotation parameter of Kerr BH giving the same ISCO radius of electrically uncharged test particles are given in Fig. 30. One can see that the RBH charge can mimic the rotation parameter up to $a = 0.8$ when the nonlinearity parameter $n = 3$; however, the for the RN BH, the charge Q_{RN} can mimic the rotation parameter up to $a \approx 0.5$. The comparison of the mimicker values of the BHs charge are in concordance with the effect of the RBH charge on the curvature of the spacetime around the BH that is stronger than for the RN BHs.

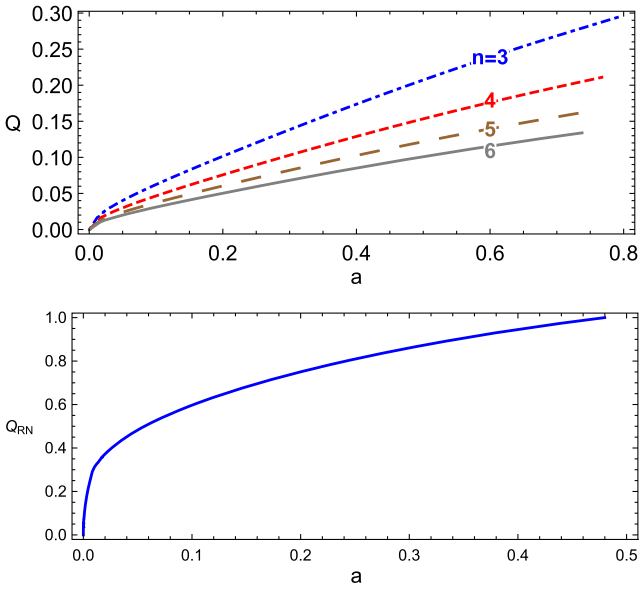

FIG. 30. The values of BH charge Q and rotation parameter a giving the same ISCO of neutral particles following the corotating orbits.

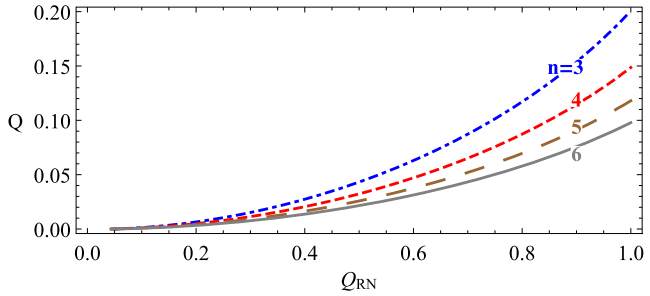

FIG. 31. The values of the RBH charge Q vs the RN BH charge Q_{RN} that imply the same ISCO radius of neutral particles are determined for characteristic values of the nonlinearity parameter n.

2. The RBH or RN BH?

Here we study relations electrically charge of RN BH and the RBH giving the same ISCO radius for test particles.

Figure 31 demonstrates the relation of the RBH Q and the RN BH Q_{RN} for the different values of the nonlinearity parameter n. One can see that the charged RN BH with $Q_{RN} \leq 1$ can mimic the RBH with the charge going up to $Q = 0.2$ for the values of ISCO radius between $4M$ and $6M$, for the parameter of nonlinearity $n = 3$. The maximal mimicker value of the RBH charge decreases with increasing value of the parameter n. Only in the cases of $r_{ISCO} \leq 4M$ the RN BHs can be distinguishable from the RBHs due to ISCO radius is minimum and it is $r_{ISCO} = 4M$ for the extreme charged RB BH. However, in such a case these ISCO orbits can be mimicked by the prograde ISCO orbits around Kerr BHs with properly chosen spin parameter a.

3. Estimations for charge of the SM RBH SrgA*

The analysis of the observed high-frequency quasiperiodic oscillations (HF-QPOs) in an x-ray band at the center of the Galaxy, whose periods are close to the period of the Keplerian accretion at the ISCO of the SMBH SrgA* with mass $(4.154 \pm 0.014) \times 10^6\ M_\odot$ have shown that the spin parameter of the SMBH $a = 0.44 \pm 0.08$ [67]. Now we can estimate the values of the NED charge of the SMBH SrgA* considering it as a RBH, which may mimic the observationally estimated value of the rotation parameter, using the agreement of the ISCO radius.

The results are given in the Table II—one can see that the mimicker values and related error bar values decrease with increasing the value of nonlinearity parameter n.

Figure 32 also illustrates the mimic values of the charge of the SMBH SrgA* when we consider it as a RBH to the spin parameter $a = 0.44 \pm 0.08$. One can see that the mimic and its error bar values decrease as the increase of the parameter of nonlinearity n.

TABLE II. Numerical mimicker values of RBH charge parameter $10^3 Q$ for the different values of the parameters n.

$n = 3$	$n = 4$	$n = 5$	$n = 6$	RNBH
$187.33^{+27.6}_{-26.4}$	$138.94^{+20.17}_{-19.15}$	$110.40^{+15.88}_{-15.01}$	$91.59^{+13.01}_{-12.35}$	$828.71^{+70.58}_{-60.94}$

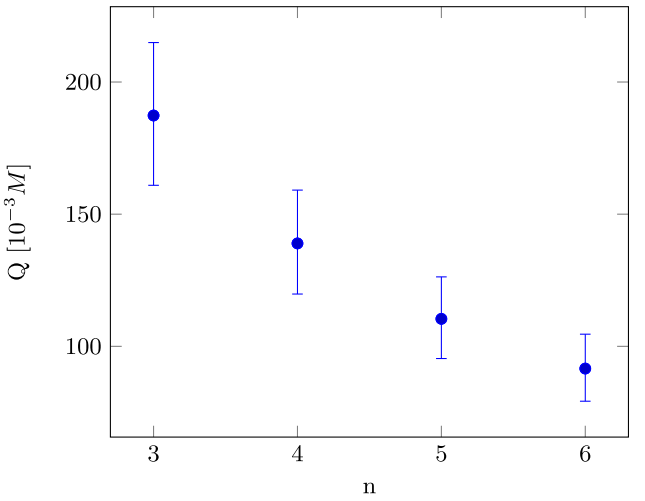

FIG. 32. Mimicker value of the charge Q of the SMBH SrgA* (considering as a RBH) the measured rotation parameter in different values of the parameter n.

VII. CONCLUSION

We studied in detail properties of the RBH spacetime obtained by coupling general relativity to nonlinear electrodynamics [1], focusing on the solutions having the proper Maxwell weak-field limit of the nonlinear model of electrodynamics. We concentrated on the properties of the spacetime curvature, the electric field, and the motion of neutral particles and electrically charged particles. The following main results were obtained.

(1) The curvature invariants of the spacetime (3) such as the Ricci scalar, square of Ricci tensor and the Kretschmann scalar have been studied. We state the following from this study.
   (a) When $n = 3$ there is finite curvature at the center of the RBH.
   (b) When $n \geq 4$ the distribution of the invariants is similar to the Gauss distribution.
   (c) The maximum value of the Ricci scalar does not depend on the value of Q but the maximum decreases as n is increased. Moreover, the maximum value of the scalar shifts outward as Q is increased.
   (d) The Kretschmann scalar and square of the Ricci tensor have similar characteristics and in the cases $n = 3$ and $n \geq 4$ the distribution of the invariants are the same as the Ricci scalar.
   (e) The maximum value of both of the invariants decreases with increasing parameters Q and n.

(2) An analytical expression for the radius of the outer event horizon for the cases of $n = 3$ and $n = 4$ was

obtained, and it was shown that the radius of the event horizon decreases as the RBH charge Q, and degree of nonlinearity n, increase. The rate at which the event horizon decreases as these parameters increase speeds up much more than in the Reissner-Nordström case.

(3) For the electric field around the RBH we can state that
   (a) an exact expression for the radial component of the electric field strength was derived. It was understood that the strength of the electric field $\mathbf{E}$ increases at large distances when $n = 3$ and as Q is increased. In extreme charged RBH case the value of $\mathbf{E}$-field becomes negative, near the event horizon.

(4) The motion of neutral particles was considered and it was shown that
   (a) the ISCO and marginally bounded radius decreases as Q and n are both increased. The rate of this decrease is larger for RBHs than in the RNBH case.
   (b) The value of the effective potential for neutral particles increases with increasing the values of the parameters Q and n.

(5) The motion of electrically charged particles around the RBH was investigated and it was shown that
   (a) the ISCO and MBO strongly depend on the RBH charge and the specific charge of the particle. For positively charged particles with $qQ < 1$, the radius of the orbits decreases as Q is increased and at $Q < Q_{\rm crit}$ ($qQ_{\rm crit} \simeq 1$) the ISCO for positively charged particles exists, but in cases when $Q \geq Q_{\rm crit}$ circular orbits do not exist due to a large repulsive Coulomb interaction;
   (b) similar effects for negatively charged particles were also seen. For small values of q the radius of ISCO and MBO decreases with increasing parameters, Q and n. With increasing values of q, the radius of ISCO and MBO reaches a minimum, then increases to a maximum and finally decreases again.
   (c) for negatively charged particles there exists ISCO at the same radius for two different values of the RBH charge. This means that even if we know about ISCO radius and value of the particle charge we cannot uniquely estimate the RBH charge.
   (d) for two oppositely charged particles having the same magnitude of specific charge there exists the same ISCO radius ($4M \leq r_{\rm ISCO} \leq 7M$) around a RBH.

(6) We have shown by comparing the radius of photon circular orbits around Kerr BH, RN BH and the RBH that:
   (a) the RBH charge may mimic the rotation parameter up to $a \approx 0.97M$ (when the parameter $n = 3$) and RN BH charge can do this mimicking up to $a \approx 0.71M$;
   (b) we have obtained the mimicker value of the RBH charge parameter as related to the rotation parameter of the SMBH M87 ($a = 0.9 \pm 0.05$) to be $10^3 Q/M = 277.564^{+3.82}_{-1.26}$ when $n = 3$, while RN BH charge mimicking is not possible.

(7) We have also shown through the comparisons of the ISCO radius of test particle around Kerr BH, RN BH and the RBH that:
   (a) the RBH charge may mimic the rotation parameter up to $a = 0.8M$ (when the parameter $n = 3$) and RN BH charge do the mimicking up to $a = 0.5M$;
   (b) the RN BH charge may mimic the RBH charge up to $Q = 0.2M$ for the case $n = 3$ and the value of the parameter n increases, the mimicking value of the charge Q decreases
   (c) the numerical analysis shows that the value of the NED charge of the regular SMBN SrgA* can mimic its spin parameter $a = 0.44 \pm 0.08$ at $10^3 Q/M = 187.33^{+27.6}_{-26.4}$ when $n = 3$, while the RN BH charge can mimic the spin parameter at $10^3 Q_{\rm RN}/M = 828.71^{+70.58}_{-60.94}$.

ACKNOWLEDGMENTS

J. R. thanks to Bobir Toshmatov, Bobur Turimov and Martin Kološ for their helpful discussions. This research is supported by Grants No. VA-FA-F-2-008, No. MRB-AN-2019-29, and No. YFA-Ftech-2018-8 of the Uzbekistan Ministry for Innovational Development, by Development internationalization of SU under the MEYS's financial contribution—indicator D and the Abdus Salam International Centre for Theoretical Physics through Grant No. OEA-NT-01. The research of the second author was supported by the United States National Science Foundation (NSF Grant No. 1826490) and the fourth author supported by Erasmus+ exchange grant between Silesian University and National University of Uzbekistan. Z. S. acknowledges Czech Science Foundation grant No. 19-03950S. J. R. thanks the Silesian University in Opava for the warm hospitality during his stay in Opava.

[1] B. Toshmatov, Z. Stuchlík, and B. Ahmedov, Phys. Rev. D **98**, 028501 (2018).
[2] H. Reissner, Ann. Phys. (Berlin) **355**, 106 (1916).
[3] G. Nordström, Proc. K. Ned. Akad. Wet., Ser. A Phys. Sci. **20**, 1238 (1918).
[4] Z. Stuchlik, Bull. Astron. Inst. Czech. **34**, 129 (1983).
[5] K. A. Bronnikov, Phys. Rev. D **63**, 044005 (2001).
[6] J. Bardeen, in *Proceedings of GR5*, edited by C. DeWitt and B. DeWitt, Tbilisi, USSR (Gordon and Breach, New York, 1968), p. 174.
[7] E. Ayón-Beato and A. García, Phys. Rev. Lett. **80**, 5056 (1998).
[8] E. Ayon-Beato, Phys. Lett. B **464**, 25 (1999).
[9] E. Ayon-Beato and A. Garcia, Gen. Relativ. Gravit. **31**, 629 (1999).
[10] C. Bambi and L. Modesto, Phys. Lett. B **721**, 329 (2013).
[11] Z.-Y. Fan and X. Wang, Phys. Rev. D **94**, 124027 (2016).
[12] B. Toshmatov, Z. Stuchlík, J. Schee, and B. Ahmedov, Phys. Rev. D **97**, 084058 (2018).
[13] B. Toshmatov, Z. Stuchlík, and B. Ahmedov, Phys. Rev. D **98**, 085021 (2018).
[14] I. Dymnikova and M. Korpusik, Phys. Lett. B **685**, 12 (2010).
[15] C. Bambi and D. Malafarina, Phys. Rev. D **88**, 064022 (2013).
[16] B. Toshmatov, B. Ahmedov, A. Abdujabbarov, and Z. Stuchlík, Phys. Rev. D **89**, 104017 (2014).
[17] I. Dymnikova and M. Khlopov, Int. J. Mod. Phys. D **24**, 1545002 (2015).
[18] I. Dymnikova and E. Galaktionov, Classical Quantum Gravity **32**, 165015 (2015).
[19] B. Toshmatov, A. Abdujabbarov, Z. Stuchlík, and B. Ahmedov, Phys. Rev. D **91**, 083008 (2015).
[20] Z. Stuchlík and J. Schee, Int. J. Mod. Phys. D **24**, 1550020 (2015).
[21] J. Schee and Z. Stuchlík, J. Cosmol. Astropart. Phys. 06 (2015) 048.
[22] A. García, E. Hackmann, J. Kunz, C. Lämmerzahl, and A. Macías, J. Math. Phys. (N.Y.) **56**, 032501 (2015).
[23] I. Dymnikova, Gravitation Cosmol. **24**, 13 (2018).
[24] I. Dymnikova and E. Galaktionov, Universe **5**, 205 (2019).
[25] I. Dymnikova and K. Kraav, Universe **5**, 163 (2019).
[26] I. Dymnikova and A. Poszwa, Classical Quantum Gravity **36**, 105002 (2019).
[27] I. Dymnikova, Int. J. Mod. Phys. A **35**, 2040053 (2020).
[28] D. N. Page, Astrophys. J. **653**, 1400 (2006).
[29] Z. Stuchlík, M. Kološ, and A. Tursunov, Proceedings **17**, 13 (2019).
[30] Z. Stuchlík, M. Kološ, J. Kovář, P. Slaný, and A. Tursunov, Universe **6**, 26 (2020).
[31] M. Zajaček and A. Tursunov, arXiv:1904.04654.
[32] M. Zajaček, A. Tursunov, A. Eckart, S. Britzen, E. Hackmann, V. Karas, Z. Stuchlík, B. Czerny, and J. A. Zensus, arXiv:1812.03574.
[33] M. Zajaček, A. Tursunov, A. Eckart, and S. Britzen, Mon. Not. R. Astron. Soc. **480**, 4408 (2018).
[34] A. Tursunov, M. Zajaček, A. Eckart, M. Kološ, S. Britzen, Z. Stuchlík, B. Czerny, and V. Karas, arXiv:1912.08174.
[35] M. Kološ, Z. Stuchlík, and A. Tursunov, Classical Quantum Gravity **32**, 165009 (2015).
[36] Z. Stuchlík and M. Kološ, Eur. Phys. J. C **76**, 32 (2016).
[37] A. Tursunov, Z. Stuchlík, and M. Kološ, Phys. Rev. D **93**, 084012 (2016).
[38] M. Kološ, A. Tursunov, and Z. Stuchlík, Eur. Phys. J. C **77**, 860 (2017).
[39] A. Tursunov, M. Kološ, Z. Stuchlík, and D. V. Gal'tsov, Astrophys. J. **861**, 2 (2018).
[40] N. Dadhich, A. Tursunov, B. Ahmedov, and Z. Stuchlík, Mon. Not. R. Astron. Soc. **478**, L89 (2018).
[41] R. Pánis, M. Kološ, and Z. Stuchlík, Eur. Phys. J. C **79**, 479 (2019).
[42] C. A. Benavides-Gallego, A. Abdujabbarov, D. Malafarina, B. Ahmedov, and C. Bambi, Phys. Rev. D **99**, 044012 (2019).
[43] B. Narzilloev, A. Abdujabbarov, C. Bambi, and B. Ahmedov, Phys. Rev. D **99**, 104009 (2019).
[44] S. Shaymatov, B. Ahmedov, Z. Stuchlík, and A. Abdujabbarov, Int. J. Mod. Phys. D **27**, 1850088 (2018).
[45] A. Abdujabbarov, N. Dadhich, and B. Ahmedov, arXiv: 1810.08066.
[46] A. A. Abdujabbarov and B. J. Ahmedov, Astrophys. Space Sci. **321**, 225 (2009).
[47] A. A. Abdujabbarov, A. A. Tursunov, B. J. Ahmedov, and A. Kuvatov, Astrophys. Space Sci. **343**, 173 (2013).
[48] A. Tursunov, M. Kološ, A. Abdujabbarov, B. Ahmedov, and Z. Stuchlík, Phys. Rev. D **88**, 124001 (2013).
[49] A. N. Aliev, Phys. Rev. D **74**, 024011 (2006).
[50] Z. Stuchlík and J. Schee, Eur. Phys. J. C **79**, 44 (2019).
[51] Z. Stuchlík, P. Slaný, and S. Hledík, Astron. Astrophys. **363**, 425 (2000).
[52] D. Pugliese, H. Quevedo, and R. Ruffini, Phys. Rev. D **83**, 104052 (2011).
[53] D. Pugliese, H. Quevedo, and R. Ruffini, Phys. Rev. D **83**, 104052 (2011).
[54] Z. Stuchlík and A. Kotrlová, Gen. Relativ. Gravit. **41**, 1305 (2009).
[55] M. Blaschke and Z. Stuchlík, Phys. Rev. D **94**, 086006 (2016).
[56] Z. Stuchlík, M. Blaschke, and J. Schee, Phys. Rev. D **96**, 104050 (2017).
[57] V. Frolov and D. Stojković, Phys. Rev. D **68**, 064011 (2003).
[58] O. G. Rahimov, Mod. Phys. Lett. A **26**, 399 (2011).
[59] O. G. Rahimov, A. A. Abdujabbarov, and B. J. Ahmedov, Astrophys. Space Sci. **335**, 499 (2011).
[60] B. Toshmatov, A. Abdujabbarov, B. Ahmedov, and Z. Stuchlík, Astrophys. Space Sci. **360**, 19 (2015).
[61] J. R. Rayimbaev, Astrophys. Space Sci. **361**, 288 (2016).
[62] K. Haydarov, A. Abdujabbarov, J. Rayimbaev, and B. Ahmedov, Universe **6**, 44 (2020).
[63] J. Vrba, A. Abdujabbarov, A. Tursunov, B. Ahmedov, and Z. Stuchlík, Eur. Phys. J. C **79**, 778 (2019).
[64] F. Tamburini, B. Thidé, and M. Della Valle, Mon. Not. R. Astron. Soc. **492**, L22 (2020).
[65] R. A. Remillard and J. E. McClintock, Annu. Rev. Astron. Astrophys. **44**, 49 (2006).
[66] R. Shafee, J. E. McClintock, R. Narayan, S. W. Davis, L.-X. Li, and R. A. Remillard, Astrophys. J. Lett. **636**, L113 (2006).

[67] Y. Kato, M. Miyoshi, R. Takahashi, H. Negoro, and R. Matsumoto, Mon. Not. R. Astron. Soc. **403**, L74 (2010).
[68] C. Bambi, K. Freese, S. Vagnozzi, and L. Visinelli, Phys. Rev. D **100**, 044057 (2019).
[69] A. Allahyari, M. Khodadi, S. Vagnozzi, and D. F. Mota, J. Cosmol. Astropart. Phys. 02 (2020) 003.
[70] Z. Stuchlík, J. Schee, and D. Ovchinnikov, Astrophys. J. **887**, 145 (2019).
[71] J. Schee and Z. Stuchlík, Eur. Phys. J. C **79**, 988 (2019).
[72] J. Schee and Z. Stuchlík, Astrophys. J. **874**, 12 (2019).
[73] B. Toshmatov, Z. Stuchlík, B. Ahmedov, and D. Malafarina, Phys. Rev. D **99**, 064043 (2019).
[74] M. Novello, V. A. de Lorenci, J. M. Salim, and R. Klippert, Phys. Rev. D **61**, 045001 (2000).
[75] I. Dymnikova, Classical Quantum Gravity **21**, 4417 (2004).
[76] Z. Stuchlík, S. Hledík, and J. Jurán, Classical Quantum Gravity **17**, 2691 (2000).
[77] Z. Stuchlík and S. Hledík, Classical Quantum Gravity **17**, 4541 (2000).
[78] J. Kovář and Z. Stuchlík, Classical Quantum Gravity **24**, 565 (2007).
[79] R. A. Konoplya and Z. Stuchlík, Phys. Lett. B **771**, 597 (2017).
[80] C. W. Misner, K. S. Thorne, and J. A. Wheeler, Gravitation Cosmol. (1973).
[81] I. D. Novikov and K. S. Thorne, in *Black Holes (Les Astres Occlus)*, edited by C. Dewitt and B. S. Dewitt (Gordon & Breach, New York, 1973), pp. 343–450.
[82] M. A. Abramowicz and P. C. Fragile, Living Rev. Relativity **16**, 1 (2013).
[83] B. Paczynsky and P. J. Wiita, Astron. Astrophys. **88**, 23 (1980).
[84] Z. Stuchlík and S. Hledík, Phys. Rev. D **60**, 044006 (1999).
[85] Z. Stuchlík, Mod. Phys. Lett. A **20**, 561 (2005).
[86] V. Balek, J. Bicak, and Z. Stuchlik, Bull. Astron. Inst. Czech. **40**, 133 (1989).
[87] Z. Stuchlík, D. Charbulák, and J. Schee, Eur. Phys. J. C **78**, 180 (2018).
[88] J. M. Bardeen, W. H. Press, and S. A. Teukolsky, Astrophys. J. **178**, 347 (1972).
[89] R. Shafee, J. E. McClintock, R. Narayan, S. W. Davis, L.-X. Li, and R. A. Remillard, Astrophys. J. Lett. **636**, L113 (2006).